Newtonian and non–Newtonian Flows into Deformable Porous Materials

A dissertation submitted in partial fulfillment of the requirements for the degree of Doctor of Philosophy at George Mason University

By

Javed Iqbal Siddique
Master of Science
Western Illinois University, 2004
Master of Philosophy
Quaid-i-Azam University, Islamabad, Pakistan, 2001
Master of Science
Azad Jammu & Kashmir University, Muzaffarabad, Pakistan, 1998

Director: Dr. Daniel M. Anderson, Associate Professor
Department of Mathematical Sciences

Summer Semester 2009
George Mason University
Fairfax, VA

Dedication

This dissertation is dedicated to my mother and father.

Acknowledgments

I would like to thank my advisor Dr. Daniel M. Anderson for his guidance, assistance, suggestions and mentoring. His patience and support in preparing this dissertation were remarkable. His help in introducing me to other members of the scientific community is and will continue to be invaluable.

I express my gratitude to my committee members Dr. T. Wanner, Dr. J. Lin and Dr. J. Cebral for their comments and suggestions. I would also like to thank Dr. P. Seshaiyer for his valuable comments and suggestions.

Special thanks goes to Drs. A. M. Siddiqui and A. Q. M. Khaliq for their advice and moral support. I would also like to thank my fellow students: Robert, Scott, Tim, Andy, Catherine, Jill, James, Faisal, and Kara. I would also like to thank my family and friends who helped and supported me. I would especially like to thank my parents and brother for all their guidance and emotional support.

Of course, I would like to deeply thank my wife for her support, and willingness to put her dreams on hold.

Table of Contents

List of Tables

List of Figures

Abstract

NEWTONIAN AND NON–NEWTONIAN FLOWS INTO DEFORMABLE POROUS MATERIALS

Javed Iqbal Siddique, PhD

George Mason University, 2009

Dissertation Director: Dr. Daniel M. Anderson

In this dissertation we examine fluid flow of Newtonian and non–Newtonian fluid into deformable porous materials. The one dimensional free boundary problems are modeled using mixture theory.

The first problem we examine in this category of flows is a mathematical model for capillary rise of a fluid into an initially dry and deformable porous material. We use mixture theory to formulate the model. We obtain analytic results for steady state positions of the wet porous material–dry porous material interface as well as liquid–wet material interface. The time-dependent free-boundary problem is solved numerically and the results compared to the steady state predictions. In the absence of gravity, the liquid rises to an infinite height and the porous material deforms to an infinite depth, following square-root in time scaling. In contrast, in the presence of gravity, the liquid rises to a finite height and porous material deforms to a finite depth. Dependence on model parameters such as the solid liquid density ratio is also explored. We also examine the one–dimensional drainage of an incompressible liquid into an initially dry and deformable porous material. Here, we identify numerical solutions that quantify the effects of gravity, capillarity and solid to liquid density ratio on the time required for a finite volume of liquid to drain into a deformable porous material.

We also study the capillary rise of a non–Newtonian liquid into a rigid and deformable porous materials in the presence and in the absence of gravity effects. In the case of rigid porous materials when gravity effects are present in the model, equilibrium heights are reached for both Newtonian and non-Newtonian cases. The evolution towards the equilibrium solution differs between Newtonian and non-Newtonian cases. In the case of deformable porous material where both fluid and solid phases move, we use mixture theory to formulate the problem. In contrast to the rigid porous materials where there is only one moving boundary, here both solid and liquid interface moves. In the absence of gravity effects, the model admits a similarity solution, which we compute numerically. If the effects of gravity are included, the free boundary problem is solved numerically where numerically computed zero gravity solution is used as an initial condition. In this case, the liquid rises to a finite height and the porous material deforms to a finite depth, following a scaling law that depends on the power law index n and power law consistency index μ^*. In this case, steady state solutions exist and are the same for both Newtonian and non-Newtonian cases.

We finally model a problem of fluid flow interactions within a deformable arterial wall. Again we use mixture theory to compute both the structural displacement of the solid and fluid motion. The coupled system of equations is solved numerically. We compare the mixture theory model to a hierarchy of models including simple spring models as well as elastic deformation models. The applications of the model are to understand the deformation of the wall as a function of its material properties and the relation of this deformation to the growth and rupture of aneurysms.

Chapter 1: Introduction

The goal of this dissertation is to study fluid flow of Newtonian and non–Newtonian into deformable porous materials. In all of the cases we have used mixture theory to model the problems.

The phenomena of capillary rise of Newtonian and non–Newtonian fluid occurs in a wide range of applications such as oil recovery, inkjet printing, textile manufacturing, medical science and geological flows. We also develop a mathematical model to study the fluid flow interaction within a deformable arterial wall using mixture theory.

- In Chapter 2, we study the capillary rise of liquid into deformable porous materials. The free boundary problem is modeled using the biphasic mixture theory approach. We first compute the steady state solutions and then compute the numerical solution of the full time dependent problem. In the absence of gravity effects the problem admits the similarity solution which we use as an initial condition for the time dependent problem. We use method of lines approach with a second order accurate finite difference scheme in space. This converts the PDE to a system of ODEs. Finally, we use MATLAB's ode23s solver to solver these ODEs along with ODEs for interface positions.

- In Chapter 3, we extend the results from Chapter 2 to study the capillary rise of non–Newtonian liquid into porous material. In the case of rigid porous material we compute the analytical solution in the absence of gravity effects and numerical solution in the presence of gravity effects. For deformable porous material case in the absence of gravity effects we introduce similarity variable that changes PDE to ODE and ODE's for interface position into a non–linear equations. We use the mid point rule and central difference to discretize the ODE, which results in system of

non-linear equations. This system of non–linear equations is solved numerically using Newton's method. To compute the solution in the presence of gravity effects we use this numerically computed similarity solution as an initial condition. Then we use method of lines to compute the solution of the full problem.

- In Chapter 4, we develop a mathematical model of fluid flow interactions within a deformable arterial wall. Here again we use mixture theory to model the problem. We use finite difference scheme to discretize the coupled system of equations. The resultant system of differential algebraic equations (DAEs) are solved numerically. We compare our mixture theory results to the elastic membrane problem on fixed and elastic membrane problem on moving domain. The applications of the model are to understand the deformation of the wall as a function of its material properties and the relation of this deformation to the growth and rupture of aneurysms.

Chapter 2: Capillary Rise into Deformable Porous Materials

2.1   Introduction

In this chapter we develop a model for capillary rise into a deformable porous material. Capillary rise phenomena occur in both rigid and deformable materials in a wide variety of scientific fields such as oil recovery, inkjet printing, textiles engineering, and flows in biological tissues. There is interest in this subject from the point of view of both industrial research and fundamental science. The present work addresses modeling and solutions of this problem that contribute to a better understanding of capillary rise into deformable porous materials.

The pioneering study of Washburn [64] described fluid flow into a rigid porous material. This model was based on the assumption that the porous material was a collection of small cylindrical capillaries, and the flow through these capillaries was Poiseuille flow subject to a pressure difference acting to force the liquid in the capillaries. In the absence of gravity, the volume of the liquid that penetrates into the porous material in a time t is proportional to $\sqrt{t}$. In contrast, when gravity is present the liquid rises to a finite, equilibrium height. The Washburn model has been widely used to describe capillary rise phenomena in rigid nondeformable porous materials.

Recently, Zhmud, *et al.* [66] studied the dynamics of capillary rise in rigid porous materials. They showed that a number of models, including the Washburn model, describing dynamics of capillary rise can be obtained as particular limiting cases of a more general equation based on Newtonian dynamics. They also showed that these general equations were in qualitative agreement with their experimental results.

However, other recent experimental investigations have revealed capillary rise behavior in rigid porous materials that departs notably from the Washburn predictions. Delker *et*

al. [23] performed experiments on capillary rise of water through a packing of glass beads. Their early time data for capillary rise height follows a $t^{1/2}$ power law, but for longer times the advancing front rises beyond the Washburn equilibrium height. Lago and Araujo [46] also observed similar dynamics in their experiments of capillary rise in an array of packed spheres. Both studies identified a new power law scaling for this longer time regime that was close to $t^{1/4}$.

Davis and Hocking [21; 22] have considered a variety of models for liquid spreading and imbibition into a rigid porous base. In their first model [21] they assumed that the porous material was uniform and isotropic in structure. The flow in the porous substrate was described by Darcy's law. In this model they considered the partially saturated case in which the wetted portion of the substrate was assumed to extend to the bottom of the porous substrate. In their second model [22] they extended their previous work to include spreading above an initially dry porous substrate. In this model they assumed that there was no cross linking of the capillaries in the substrate which was also the case in the Washburn model. They calculated the penetration shapes as a function of time.

The above discussion outlines briefly some of the classical as well as more recent studies involving flows in rigid porous materials. Here we turn our attention to porous materials which deform when liquid passes through them, e.g sponge–like materials. Deformable porous materials arise in various fields, including geophysics [61], soil science [41; 42; 54], infiltration [2; 10; 49; 57; 60] snow physics [26], paper and printing [18; 27], and medical science [6; 7; 8; 33; 34; 35; 36; 37; 38]. In such cases, the flow through the deformable porous media deforms the material due to the forces associated with flow. The material deformation in turn influences the flow. Models that account for both flow and deformation are required to analyze the dynamics of these materials.

Early models of flows in deformable porous media were developed to study soil consolidation. Biot [12] described a problem involving deformable porous media in which Darcy's law, used to describe the fluid flow, was coupled to a linear elasticity model for the solid deformation. He presented the solutions for soil consolidation in one dimension as well as

two dimensions under permeable [11] and impermeable [13] rectangular loads.

Our approach follows more recent work in which the porous material is modeled as a mixture of solid and fluid. In mixture theory each component is treated as a single continuum and every point in space is considered to be occupied by a particle belonging to each component of the mixture at each instant of time. A detailed mixture theory description is presented by several authors [4; 15].

Barry and Aldis [6; 7] examined a variety of different models of deformable porous media based on mixture theory. These models include cases of flow induced deformation from pressurized cavities in absorbing porous tissues and radial flow through deformable porous shells. In their flow induced deformation model, biological tissues are modeled as nonlinear deformable porous media where the deformation of the tissues in turn alters the flow. In the case of radial flow, a governing system of equations was developed for cylindrical and spherical geometries.

Hou *et al.* [38] studied the formulation of boundary conditions between a viscous fluid and a biphasic mixture. They used binary mixture theory to develop a set of boundary conditions based on conservation laws. These conditions were validated by applying them to Poisuelle flow and Couette flow problems.

Barry *et al.* [8] revisited the work of Hou *et al.* [38] for fluid flow over a thin deformable porous layer. Binary mixture theory was used to obtain the governing system of equations with assumptions that solid deformation was infinitesimal and the predominant displacement was along the axis of the channel. Wang and Parker [63] examined the effect of deformable porous surface layers on the motion of a sphere in a narrow cylindrical tube. They also used binary mixture theory for solid and liquid constituents to model the porous layer on both the surface of the tube and the sphere. They applied lubrication theory in the region between the sphere and the wall in order to study the effects of deformable layers on the motion of the sphere.

Sommer and Mortensen [60] considered the forced unidirectional infiltration in an initially dry deformable porous material. A constant applied pressure drove the fluid flow

in the porous material. Agreement between their model and the experimental results was reported.

Preziosi *et al.* [57] studied the infiltration of a liquid into a deformable porous material. In this model, an initially dry and compressed porous material was infiltrated by an incompressible liquid which caused the porous material to deform and relax.

Following this work, Anderson [3] presented a model for the imbibition of a liquid droplet on a deformable porous substrate using the deformation model of Preziosi *et al.* For the assumed one–dimensional material deformation, a model for the imbibition of liquid into the porous material and also for the porous material deformation was developed. Anderson's model, which did not include gravitational effects, predicted that during the imbibition of liquid into the deformable porous substrate, swelling, swelling-relaxation and shrinking of the porous material could occur.

The ideas used for modeling deformable sponge-like materials also have application to problems involving suspensions and gels. Manley *et al.* [48] performed experiments and examined a model for gravitational collapse of colloidal gels. Their model was based on a Darcy's equation similar to the one we use here. Approximations, such as negligible fluid velocity relative to the solid velocity and constant solid volume fraction lead to a gel height that decays exponentially in time to an equilibrium height determined by a balance of gravitational and elastic forces. Kim *et al.* [44] examine a similar problem that addresses gravitational collapse and stabilization of a suspension of attractive colloidal particles. Their mathematical model is very similar to ours but differs in details including boundary conditions as we discuss further in the next section.

Dufresne *et al.* [24; 25] studied related systems involving the flow and fracture in drying nano–particle suspensions. Here the compaction of the material is driven by evaporation and fluid flow at the drying surface. The dynamics of the compaction front, crack formation in the drying suspension and long time crack propagation were investigated.

In the present work, we consider capillary rise of a fluid into a deformable porous material. Our model is an analog of the Washburn model [64] of capillary rise into a rigid

6

porous material. The basic governing equations for flow in deformable material follow those of several previous authors [3; 6; 7; 35; 57; 60]. Our model follows most closely that of Preziosi *et al.*[57], Barry and Aldis [6; 7] and Anderson [3]. We are interested in examining gravitational effects; these have been included in previous models [7; 8; 57], but the corresponding solutions have not been addressed.

In section two we present the one-dimensional capillary rise problem and then non-dimensionalize the governing system of equations. In section three, we present equilibrium and time-dependent solutions of the capillary rise problem. In section four results and discussion of the capillary rise problem are given. In section five we discuss the drainage problem and its solutions. Section six contains the conclusions.

2.2 The Model

We use mixture theory [2; 6; 7] to formulate the problem of capillary rise into a deformable porous material. The mixture under consideration consists of a fluid and a deformable solid material. Mixture theory is a homogenization approach in which each component is treated as a single continuum and every point in space is considered to be occupied by a particle belonging to each component of the mixture at each instant of time. As a Newtonian and incompressible fluid flows through a deformable material, the porous material deforms altering the porosity and permeability, which effects the flow of fluid in the porous deformable material.

In this section we describe the governing equations in the deformable material. In the section that follows we discuss the boundary conditions appropriate for our specific geometry. The procedure used here follows that of [7]. The velocities of liquid and solid phases are denoted by $\vec{w}_\ell$ and $\vec{w}_s$ respectively. The apparent liquid and solid densities in an infinitesimally small volume dv are

$$\rho_s^a = \lim_{dv \to 0} \frac{dm_s}{dv}, \qquad \rho_\ell^a = \lim_{dv \to 0} \frac{dm_\ell}{dv}, \tag{2.1}$$

7

where dm_s and dm_ℓ are solid and liquid phase masses in dv. The true intrinsic densities of solid and liquid material phases are

$$\rho_s = \lim_{dv_s \to 0} \frac{dm_s}{dv_s}, \qquad \rho_\ell = \lim_{dv_\ell \to 0} \frac{dm_\ell}{dv_\ell}, \tag{2.2}$$

where dv_s and dv_ℓ are the small volumes occupied by solid and liquid phase respectively. The solid and liquid volume fractions are

$$\phi = \lim_{dv \to 0} \frac{dv_s}{dv}, \qquad 1 - \phi = \lim_{dv \to 0} \frac{dv_\ell}{dv}. \tag{2.3}$$

From the above equations we infer that

$$\rho_s^a = \phi \rho_s, \qquad \rho_\ell^a = (1 - \phi)\rho_\ell. \tag{2.4}$$

The mixture density can be written from the following formula

$$\rho^t = \lim_{dv \to 0} \frac{dm}{dv} = \lim_{dv \to 0} \frac{dm_s + dm_\ell}{dv}, \tag{2.5}$$

so that

$$\rho^t = \rho_s^a + \rho_\ell^a = \phi \rho_s + (1 - \phi)\rho_\ell. \tag{2.6}$$

The mass balance for both liquid and solid phases for constant ρ_s and ρ_ℓ after using (2.4) can be written as follows

$$\frac{\partial \phi}{\partial t} + \nabla \cdot (\phi \vec{w}_s) = 0, \tag{2.7}$$

$$-\frac{\partial \phi}{\partial t} + \nabla \cdot [(1 - \phi)\vec{w}_\ell] = 0. \tag{2.8}$$

8

The momentum balance for liquid and solid constituents are

$$\rho_s \phi \left(\frac{\partial \vec{w}_s}{\partial t} + \vec{w}_s \cdot \nabla \vec{w}_s \right) = \nabla \cdot \mathbf{T}_s + \phi \rho_s \vec{g} + \vec{\pi}_s, \tag{2.9}$$

$$\rho_\ell (1 - \phi) \left(\frac{\partial \vec{w}_\ell}{\partial t} + \vec{w}_\ell \cdot \nabla \vec{w}_\ell \right) = \nabla \cdot \mathbf{T}_\ell + \rho_\ell (1 - \phi) \vec{g} + \vec{\pi}_\ell, \tag{2.10}$$

where $\mathbf{T}_s$ and $\mathbf{T}_\ell$ are stress tensors for solid and liquid phases, $\vec{g}$ is gravity and $\vec{\pi}_s$ and $\vec{\pi}_\ell$ are drag forces.

We will neglect the inertial terms in equations (2.9) and (2.10) due to the assumption that the fluid velocities and deformation rates are small. Also, Newton's third law requires that the force on the solid by the liquid is opposite to that on the liquid by the solid $\vec{\pi}_\ell = -\vec{\pi}_s$. We follow Barry and Aldis [6] and write the stress tensors and drag forces as

$$\mathbf{T}_s = -\phi p \mathbf{I} + \sigma_s, \qquad \mathbf{T}_\ell = -(1 - \phi) p \mathbf{I} + \sigma_\ell, \tag{2.11}$$

$$\vec{\pi}_\ell = -\vec{\pi}_s = \frac{(1 - \phi)^2 \mu}{K(\phi)} (\vec{w}_s - \vec{w}_\ell) - p \nabla \phi, \tag{2.12}$$

where σ_s and σ_ℓ are solid and liquid stresses, p is the pressure and $\mathbf{I}$ is the identity tensor. If the fluid stress σ_ℓ is neglected and $\sigma_s = \sigma$, the system of equation (2.7)–(2.10) reduces to

$$\frac{\partial \phi}{\partial t} + \nabla \cdot (\phi \vec{w}_s) = 0, \tag{2.13}$$

$$\frac{\partial \phi}{\partial t} - \nabla \cdot ((1 - \phi) \vec{w}_\ell) = 0, \tag{2.14}$$

$$\vec{w}_s - \vec{w}_\ell = \frac{K(\phi)}{(1 - \phi)\mu} (\nabla p - \rho_\ell \vec{g}), \tag{2.15}$$

$$\nabla \cdot \sigma = \nabla p - (\rho_s \phi + (1 - \phi) \rho_\ell) \vec{g}. \tag{2.16}$$

$\leftarrow$Porous Material

$h_\ell(t)$ $p = p_A + p_c$

Wet Material$\rightarrow$ $\leftarrow p(z=0) = p_A$

$h_s(t)$ $p = p_A - \rho_\ell g h_s$

$\leftarrow$Liquid
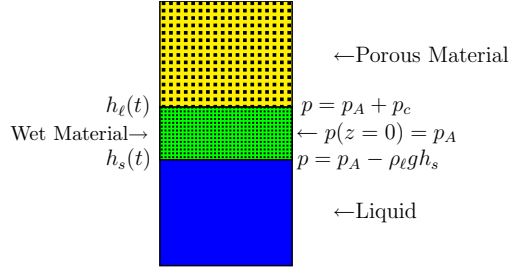
Figure 2.1: This figure shows the one dimensional capillary rise configuration

Equations (2.13)–(2.16) are the governing system of equations for flow in a deformable porous material, subject to boundary conditions outlined below.

2.3 One–dimensional capillary rise into a deformable porous material

In the following, we consider a one dimensional problem where we can examine solutions to the above equations. In particular, we consider a deformable sponge-like material in contact with a liquid. The upper end of the deformable material is fixed. At time $t = 0$, the contact position of the deformable material and liquid is defined by $z = 0$. It is assumed that the imbibition of fluid occurs from an infinite bath of fluid whose upper surface at $z = 0$ remains open to atmospheric pressure (i.e. $p = p_A$ at $z = 0$ for all time). For $t > 0$ the liquid rises into an initially dry porous material due to capillary suction in the pore space of the porous material assuming the capillary pressure $p_c < 0$, which results in deformation of the porous material. The upper interface of the wet porous material region is defined by $z = h_\ell(t)$ and the lower interface formed after the deformation is defined by $z = h_s(t)$ as shown in figure 2.1. We have assumed that the pressure in the fluid bath is hydrostatic. This implies that $p = p_A - \rho_\ell g h_s$ at $z = h_s(t)$. The dry porous material is rigid and has uniform solid fraction ϕ_0. As a result of the above assumptions, the only remaining unknowns are those in the wet material and the boundary positions h_s and h_ℓ. The variables of interest in the

wet region are the solid fraction ϕ, the vertical velocity component of the liquid phase w_ℓ, the vertical velocity component of solid phase w_s, the liquid pressure p and the stress in the solid σ where $\sigma = \sigma\mathbf{I}$. The set of equations for the one dimensional material deformation can be written as

$$\frac{\partial \phi}{\partial t} + \frac{\partial}{\partial z}(\phi w_s) = 0, \tag{2.17}$$

$$\frac{\partial \phi}{\partial t} - \frac{\partial}{\partial z}[(1 - \phi)w_\ell] = 0, \tag{2.18}$$

$$w_\ell - w_s = -\frac{K(\phi)}{(1 - \phi)\mu}\left(\frac{\partial p}{\partial z} + \rho_\ell g\right), \tag{2.19}$$

$$0 = -\frac{\partial p}{\partial z} + \frac{\partial \sigma}{\partial z} - g\left[\rho_s \phi + \rho_\ell(1 - \phi)\right], \tag{2.20}$$

where ρ_s and ρ_ℓ are the true intrinsic densities of solid and liquid respectively and are assumed to be constant. The permeability $K(\phi)$ and solid stress $\sigma(\phi)$, whose forms we specify below, are functions of the local solid volume fraction, μ is the dynamic viscosity and g is the gravitational acceleration. Equations (2.17)–(2.20) are consistent with those of previous authors [6; 7; 57]. More specifically, equation (2.17) and (2.18) are the mass balance equations for solid and liquid phases respectively where the assumption of constant density has been taken into account. Equations (2.19) and (2.20) are reduced from general solid and liquid momentum balances (e.g. see Preziosi *et al.* equations (3) and (4)). In particular, our equation (2.20) represents a combined momentum balance of the fluid–solid mixture. Note that we have assumed that inertial terms and viscous stresses are negligible and that stress tensors and frictional forces between phases take forms standard in mixture theory (e.g. see equations (16) and (17) in Barry and Aldis [7]). In this case the only velocity terms in the momentum balances appear in the relative velocity of the modified Darcy equation (2.19). Our new contribution is to examine in detail solutions of these equations, and boundary conditions we specify below, in order to assess gravitational effects on the flow and deformation.

Equations (2.17)–(2.20) can be reduced to a single partial differential equation for the solid fraction ϕ, as in [3]. Subtracting equation (2.18) from equation (2.17), and integrating once gives

$$\phi w_s + (1 - \phi)w_\ell = c(t), \tag{2.21}$$

where $c(t)$ is a function determined by the boundary conditions. Equations (2.19) and (2.21) allow us to write formulas for liquid and solid velocities as follows

$$w_\ell = c(t) - \frac{\phi K(\phi)}{(1 - \phi)\mu}\left(\frac{\partial p}{\partial z} + \rho_\ell g\right), \tag{2.22}$$

$$w_s = c(t) + \frac{K(\phi)}{\mu}\left(\frac{\partial p}{\partial z} + \rho_\ell g\right). \tag{2.23}$$

Since the stress is a function of the solid volume fraction $\sigma = \sigma(\phi)$ equation (2.20) can be written as follows

$$\frac{\partial p}{\partial z} = \sigma'(\phi)\frac{\partial \phi}{\partial z} - g[\rho_s \phi + \rho_\ell(1 - \phi)]. \tag{2.24}$$

After combining equations (2.17), (2.23) and (2.24), we get the equation for ϕ

$$\frac{\partial \phi}{\partial t} + c(t)\frac{\partial \phi}{\partial z} = -\frac{\partial}{\partial z}\left[\frac{\phi K(\phi)}{\mu}\left\{\sigma'(\phi)\frac{\partial \phi}{\partial z} - g(\rho_s - \rho_\ell)\phi\right\}\right], \tag{2.25}$$

on $h_s(t) < z < h_\ell(t)$. When gravity is absent, equation (2.25) is equivalent to equation (44) in Prezoisi et al. [57] and equation (20) in Anderson [3]. When gravity is absent, equation (2.25) is equivalent to equation (44) in Prezoisi *et al.* [57] and equation (20) in Anderson [3]. The same PDE for ϕ can be seen in the work of Kim *et al.*[44] by interpreting our $K(\phi)$ as their $\kappa(\phi)$, our μ as their η, our $\sigma'(\phi)$ as their $-K(\phi)/\phi$ and our $c(t) = 0$. The case $c(t) = 0$ follows if the solid and liquid velocities are zero at the bottom boundary, as in Kim *et al.* While their final equation is the same as ours, we note that their stress

balance (their equation 5) and continuity equation (their equation 6) involve $\partial p / \partial z$ rather than $\partial p / \partial z + \rho_\ell g$.

The boundary conditions applied at the liquid-wet material interface $z = h_s(t)$ are

$$w_s\left(h_s^+, t\right) = \frac{\partial h_s}{\partial t}, \tag{2.26}$$

$$p\left(h_s^+, t\right) = p_A - \rho_\ell g h_s(t), \tag{2.27}$$

$$\sigma\left(h_s^+, t\right) = 0, \tag{2.28}$$

where p_A is atmospheric pressure. The equations (2.26)–(2.28) are the kinematic condition, hydrostatic pressure assumption in the liquid bath, and zero stress condition respectively.

The boundary conditions applied at the wet material-dry material interface $z = h_\ell(t)$ are

$$w_\ell\left(h_\ell^-, t\right) = \frac{\partial h_\ell}{\partial t}, \tag{2.29}$$

$$p\left(h_\ell^-, t\right) = p_A + p_c, \tag{2.30}$$

where p_c is a constant capillary pressure. Here (2.29) and (2.30) are kinematic and capillary pressure conditions respectively.

Following Prezoisi et al. and Anderson, an expression for the $c(t)$ can be written as

$$c(t) = -\frac{(1 - \phi_0)}{\phi_0}\left[\frac{\phi K(\phi)}{\mu(1 - \phi)}\left(\sigma'(\phi)\frac{\partial \phi}{\partial z} - g(\rho_s - \rho_\ell)\phi\right)\right]\Bigg|_{h_\ell^-}. \tag{2.31}$$

The combination of equations (2.22) through (2.24) with equations (2.26) and (2.29) yields equations for interface positions

$$\frac{\partial h_s}{\partial t} = c(t) + \frac{K(\phi)}{\mu}\left(\sigma'(\phi)\frac{\partial \phi}{\partial z} - g(\rho_s - \rho_\ell)\phi\right)\Bigg|_{h_s^+}, \tag{2.32}$$

13

$$\frac{\partial h_\ell}{\partial t} = c(t) - \frac{\phi K(\phi)}{\mu(1-\phi)} \left(\sigma'(\phi)\frac{\partial \phi}{\partial z} - g(\rho_s - \rho_\ell)\phi \right)\Bigg|_{h_\ell^-}. \tag{2.33}$$

To summarize, we need to solve (2.24) and (2.25) subject to (2.27), (2.28) and (2.30) where the free surface positions are determined by (2.32) and (2.33) along with appropriate initial conditions. Note that equation (2.25) is coupled to equation (2.24) and the pressure via the boundary conditions.

2.3.1 Nondimensionalized System of Equations

Before solving the time-dependent problem we introduce the following dimensionless quantities for space, time, interface positions and pressure

$$\bar{z} = \frac{z - h_s(t)}{h_\ell(t) - h_s(t)}, \qquad \bar{t} = \frac{t}{T}, \qquad \bar{h}_s = \frac{h_s}{L}, \qquad \bar{h}_\ell = \frac{h_\ell}{L}, \qquad \bar{p} = \frac{p}{m}, \tag{2.34}$$

where $L = \frac{m}{\rho_\ell g}$ and $T = \frac{L^2 \mu}{m K_0}$. Here K_0 and m are permeability and stress scales defined below. These choices of dimensionless variables allows us to transform the moving boundary problem to a fixed domain problem.

Our choices for permeability $K(\phi)$ and stress $\sigma(\phi)$, which are consistent with physically realistic trends, are $K(\phi) = \frac{K_0}{\phi}$, where $K_0 > 0$ and $\sigma(\phi) = m(\phi_r - \phi)$ [3]. We take $m > 0$ so that $\sigma'(\phi) = -m < 0$. The assumed form of the stress function is suitable for our one-dimensional deformation model; in higher dimensions, this would need to be generalized to account for effects such as shear deformation. Note that σ is positive for $\phi < \phi_r$ (i.e. expansion relative to the relaxed state) and negative for $\phi > \phi_r$ (i.e. compression relative to the relaxed state). According to this choice, when solid fraction is at a constant relaxed value ϕ_r, the stress function is zero.

Introducing these choices and dimensionless variables, the PDE for ϕ can be written as

$$\frac{\partial \phi}{\partial \bar{t}} + \left[\frac{(\bar{z}-1)}{(\bar{h}_\ell - \bar{h}_s)} \frac{d\bar{h}_s}{d\bar{t}} - \frac{\bar{z}}{(\bar{h}_\ell - \bar{h}_s)} \frac{d\bar{h}_\ell}{d\bar{t}} \right] \frac{\partial \phi}{\partial \bar{z}} + \frac{\bar{c}(\bar{t})}{(\bar{h}_\ell - \bar{h}_s)} \frac{\partial \phi}{\partial \bar{z}} =$$

$$\frac{1}{(\bar{h}_\ell - \bar{h}_s)^2} \frac{\partial^2 \phi}{\partial \bar{z}^2} + \frac{\rho}{(\bar{h}_\ell - \bar{h}_s)} \frac{\partial \phi}{\partial \bar{z}}, \tag{2.35}$$

where $\rho = (\frac{\rho_s}{\rho_\ell} - 1)$.

Boundary conditions for solid volume fraction can be derived from the zero stress and stress equilibrium conditions as follows

$$\phi = \phi_r, \qquad \text{at} \qquad \bar{z} = 0, \tag{2.36}$$

$$\phi = \phi_\ell^* - (\bar{h}_\ell - \bar{h}_s) \int_0^1 (\rho\phi + 1)d\bar{z} - \bar{h}_s \qquad \text{at} \qquad \bar{z} = 1, \tag{2.37}$$

where $\phi_\ell^* = \phi_r - \frac{p_c}{m}$. The boundary condition (2.37) is obtained by integrating (2.24) and applying the pressure boundary conditions (2.27) and (2.30). Note that in the absence of gravity equation (2.37) reduces to $\phi = \phi_\ell^*$. The function $\bar{c}(\bar{t})$ is given by

$$\bar{c}(\bar{t}) = \frac{1 - \phi_0}{\phi_0} \left[\frac{1}{(1-\phi)(\bar{h}_\ell - \bar{h}_s)} \frac{\partial \phi}{\partial \bar{z}} + \frac{\rho\phi}{(1-\phi)} \right]\Bigg|_{\bar{z}=1}, \tag{2.38}$$

and dimensionless interface positions satisfy the ODEs

$$\frac{d\bar{h}_s}{d\bar{t}} = \bar{c}(\bar{t}) - \left[\frac{1}{\phi(\bar{h}_\ell - \bar{h}_s)} \frac{\partial \phi}{\partial \bar{z}} + \rho \right]\Bigg|_{\bar{z}=0}, \tag{2.39}$$

$$\frac{d\bar{h}_\ell}{d\bar{t}} = \bar{c}(\bar{t}) + \left[\frac{1}{(1-\phi)(\bar{h}_\ell - \bar{h}_s)} \frac{\partial \phi}{\partial \bar{z}} + \frac{\rho\phi}{(1-\phi)} \right]\Bigg|_{\bar{z}=1}. \tag{2.40}$$

15

The initial conditions for the interface positions are

$$\bar{h}_\ell(\bar{t} = 0) = 0, \qquad \bar{h}_s(\bar{t} = 0) = 0. \tag{2.41}$$

2.4　Capillary rise solutions approach

The time dependent free boundary problem (2.35)–(2.41) can be solved numerically. First, however, we will identify the equilibrium state solution which will be compared with the time dependent solution later in the results section.

2.4.1　Steady state solution

The steady state solution for solid volume fraction and pressure can be written as follows

$$\phi(\bar{z}) = \phi_r e^{\rho(\bar{h}_s^\infty - \bar{h}_\ell^\infty)\bar{z}}, \tag{2.42}$$

and

$$\bar{p}(\bar{z}) = \phi_r - \phi_\ell^* + (\bar{h}_\ell^\infty - \bar{h}_s^\infty)(1 - \bar{z}) + \bar{p}_A, \tag{2.43}$$

where $\bar{h}_s^\infty$ and $\bar{h}_\ell^\infty$ are the equilibrium heights of solid and liquid respectively to be determined. Here $\bar{p}_A$ is dimensionless atmospheric pressure. This pressure corresponds to hydrostatic pressure and quantity $\phi_r - \phi_\ell^*$ can be interpreted as a dimensionless capillary pressure.

To find the steady state solid interface position $\bar{h}_s^\infty$, we use a global mass conservation argument which can be stated as follows. The mass of the solid before liquid is imbibed into the material is equal to the mass of the solid after liquid is imbibed into the material. In dimensionless form, this is

$$\phi_0 \bar{h}_\ell^\infty = (\bar{h}_\ell^\infty - \bar{h}_s^\infty) \int_0^1 \phi(\bar{z}) d\bar{z}. \tag{2.44}$$

The solution of equation (2.44) after using (2.42) yields a steady state solid interface position

$$\bar{h}_s^\infty = \frac{1}{\rho}\ln(1 - \rho\bar{h}_\ell^\infty\frac{\phi_0}{\phi_r}) + \bar{h}_\ell^\infty. \tag{2.45}$$

Also the steady state liquid interface position can be written as

$$\bar{h}_\ell^\infty = \phi_\ell^* - \phi_r, \tag{2.46}$$

Note that in dimensional form $h_\ell^\infty = -\frac{p_c}{\rho_\ell g}$, which is the same as that for capillary rise in a rigid porous material given the same capillary pressure p_c. Using (2.42) and (2.45) we can define

$$\phi_\ell^\infty = \phi_r - \rho(\phi_\ell^* - \phi_r)\phi_0, \tag{2.47}$$

where ϕ_ℓ^∞ is the solid volume fraction at the wet material-dry material interface evaluated in the limit $t \to \infty$. Further discussion of these solutions will be given in the results section. In the following section we will solve the time–dependent capillary rise problem.

2.4.2 Time-Dependent Solution

The coefficients of equations (2.35), (2.39) and (2.40) are singular at time $t = 0$. However, in the asymptotic limit $t \to 0$ these equations and the boundary condition (2.37) reduce to the zero gravity case. In this case, equation (2.35) with the associated boundary conditions can be solved using the similarity variable $\eta = \frac{z}{2\sqrt{Dt}}$, where $D = \frac{L^2}{T} = \frac{K_0 m}{\mu}$ has units of length squared per unit time (see [3] for details). Here the interface positions can be expressed as

$$\bar{h}_s(\bar{t}) = 2\lambda_s\sqrt{\bar{t}}, \qquad \bar{h}_\ell(\bar{t}) = 2\lambda_\ell\sqrt{\bar{t}}. \tag{2.48}$$

The zero gravity solution, denoted by $\phi_s(\eta)$, can be written in terms of the error function as follows

$$\phi_s(\eta) = \frac{\text{erf}(\lambda_s - B) - \text{erf}(\eta - B)}{\text{erf}(\lambda_s - B) - \text{erf}(\lambda_\ell - B)}(\phi_\ell^* - \phi_r) + \phi_r, \tag{2.49}$$

where

$$B = (1 - \phi_0)\lambda_\ell, \tag{2.50}$$

and

$$
\begin{aligned}
\lambda_s &= \frac{(\phi_\ell^* - \phi_r)}{\sqrt{\pi}[\text{erf}(\lambda_s - B) - \text{erf}(\lambda_\ell - B)]} \\
&\times \left\{ \frac{1}{\phi_r} \exp[-(\lambda_s - B)^2] - \frac{(1 - \phi_0)}{\phi_0(1 - \phi_\ell^*)} \exp[-(\lambda_\ell - B)^2] \right\},
\end{aligned}
\tag{2.51}
$$

$$\lambda_\ell = -\frac{(\phi_\ell^* - \phi_r)\exp[-(\lambda_\ell - B)]}{\phi_0(1 - \phi_\ell^*)\sqrt{\pi}[\text{erf}(\lambda_s - B) - \text{erf}(\lambda_\ell - B)]}. \tag{2.52}$$

This is the solution given in Anderson [3], equations (46)–(49). We avoid the singularity at $\bar{t} = 0$ (when $\bar{h}_s(\bar{t}) = \bar{h}_\ell(\bar{t}) = 0$) numerically when solving equation (2.35)–(2.40) by using this similarity solution as an initial condition at time $\bar{t} = \bar{t}_I > 0$. Specifically, the initial condition for ϕ can be derived from the similarity solution $\phi(\bar{z}, \bar{t}_I) = \phi_s(\eta)$, where $\bar{t}_I$ is chosen to be sufficiently small so that the solution is independent of any further reduction in $\bar{t}_I$. Noting that

$$\eta = \lambda_s + \bar{z}(\lambda_\ell - \lambda_s), \tag{2.53}$$

the initial condition for ϕ in dimensionless form becomes

$$\phi(\bar{z}, \bar{t} = t_I) = \phi_s(\lambda_s + \bar{z}(\lambda_\ell - \lambda_s)). \tag{2.54}$$

18
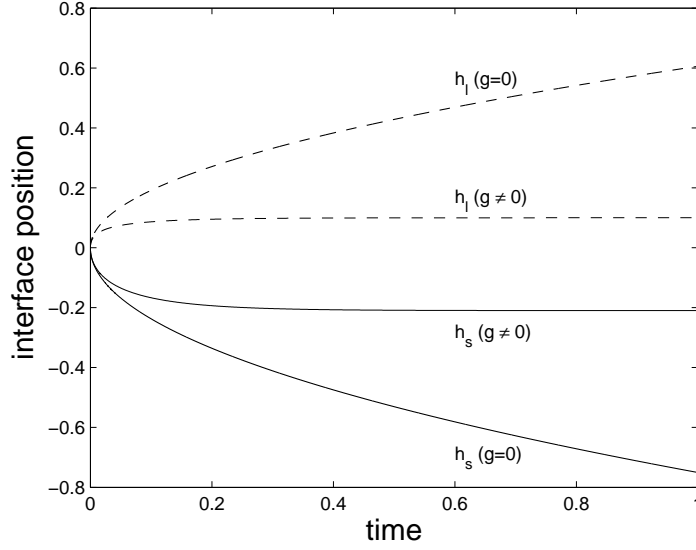
Figure 2.2: This figure shows the evolution of the interface positions h_s and h_ℓ for $g = 0$ and $g \neq 0$. In this plot we have used $\phi_\ell^* = 0.2$, $\phi_r = 0.1$, $\phi_0 = 0.33$ and for the nonzero gravity case $\rho = 0.1$.

The initial conditions for $\bar{h}_s$ and $\bar{h}_\ell$ are

$$\bar{h}_s(\bar{t}_I) = 2\lambda_s\sqrt{\bar{t}_I}, \qquad \bar{h}_\ell(\bar{t}_I) = 2\lambda_\ell\sqrt{\bar{t}_I}. \tag{2.55}$$

The above system of equations (2.35)–(2.40) is solved numerically subject to the initial conditions (2.55) and also by using the similarity solution (2.54) as an initial condition for ϕ. To compute the numerical solution, we use a method of lines approach with a 2nd order accurate finite difference scheme in space. This converts the PDE to a system of ODEs. These ODEs along with (2.39) and (2.40) are solved numerically using Matlab's ode23s solver.

2.5 Capillary rise results and discussion

Figure 2 shows the evolution of interface positions $\bar{h}_s(t)[g = 0, g \neq 0$ cases] and $\bar{h}_\ell(t)$ $[g = 0, g \neq 0$ cases]. In the absence of gravity, $\bar{h}_s(t)$ evolves downward and $\bar{h}_\ell(t)$ evolves upward following a square root in time trend. This is the similarity solution of Anderson
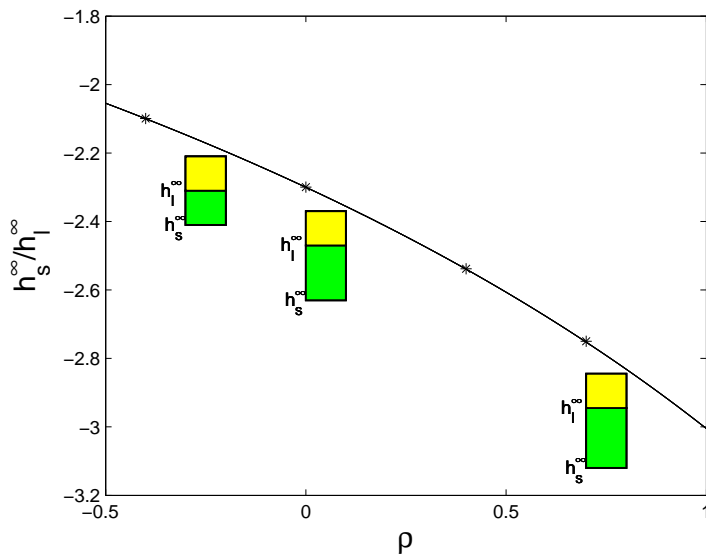
Figure 2.3: This plot shows the ratio of $\frac{\bar{h}_s^\infty}{\bar{h}_\ell^\infty}$ versus ρ given by equation (2.45). The solid line is analytical solution and $*$ is the full numerical solution at large times for different ρ values for fixed values of $\phi_r=0.10$, $\phi_0 = 0.33$ and $\phi_\ell^* = 0.20$.

[3]. For the nonzero gravity case, initially both curves follow the similarity solution but ultimately reach steady state values $\bar{h}_s^\infty$ and $\bar{h}_\ell^\infty$. The steady state values for $\bar{h}_s^\infty$, $\bar{h}_\ell^\infty$ that can be observed in Fig 2, depend on various parameters. In the next several figures we explore this dependence. We first note that the dimensionless $\bar{h}_\ell^\infty$ is independent of ρ (2.46). However, it is important to point out that the length scale L and the dimensional h_ℓ^∞ do depend on ρ_ℓ. Therefore, we interpret ρ as a dimensionless quantity measuring solid density.

In the figure 3, ratio of $\bar{h}_s^\infty$ and $\bar{h}_\ell^\infty$ is plotted as a function of ρ. The solid curve represents the analytical solution of $\bar{h}_s^\infty$ and $\bar{h}_\ell^\infty$ for ρ values ranging from -0.5 to 1. Four numerically computed values of $h_\ell(t)$ and $h_s(t)$ for sufficiently large times are also indicated along this curve, indicating agreement between numerical and analytical results. Three different one dimensional deformable material figures are also shown in this plot to represent the dependence of deformation on ρ. In particular, we observe that solid deformation increases with increasing ρ.

20
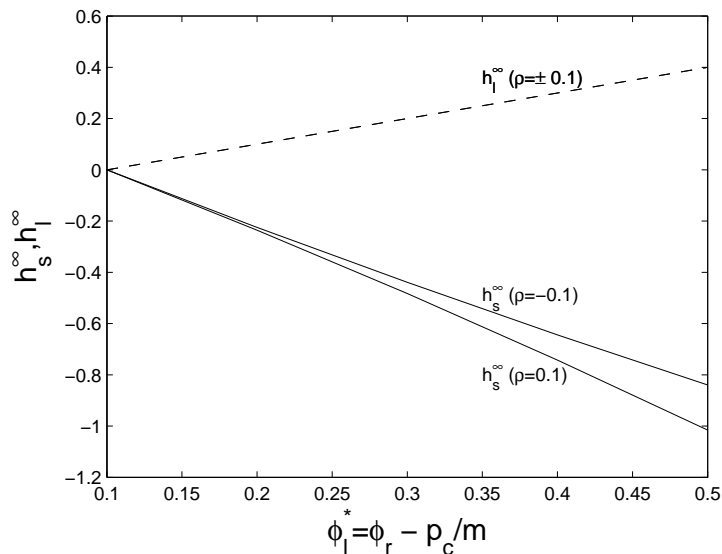
Figure 2.4: This is a plot of $\bar{h}_s^\infty$ and $\bar{h}_\ell^\infty$ as a function of ϕ_ℓ^* for $\phi_0 = 0.33$, $\phi_r = 0.1$, and $\rho = \pm 0.1$.

In Figure 4 we explore the dependence of the interface positions on the capillary pressure. First observe that when ϕ_ℓ^* is equal to ϕ_r, (i.e. capillary pressure is zero), no fluid is imbibed by the porous material; here $\bar{h}_s^\infty$, $\bar{h}_\ell^\infty$ equal zero. As the capillary suction increases (i.e. ϕ_ℓ^* increases) the porous material starts deforming. This rate of deformation depends on the value of ρ. For $\rho = -0.1$, the deformation in the porous material is smaller than compared to $\rho = 0.1$. As mentioned in the discussion of figure 3, the height of fluid $\bar{h}_\ell^\infty$ depends linearly on ϕ_ℓ^* [see also equation (2.45)].

Figure 5 shows a plot of $\bar{h}_s^\infty$, $\bar{h}_\ell^\infty$ versus ϕ_r for different values of ϕ_0. Note that $\bar{h}_\ell^\infty$, indicated by the dashed line, is independent of ϕ_0. Situations of net compression ($\bar{h}_s^\infty$ positive) generally correspond to relatively small values of ϕ_0. In order for this to be physically realistic, we assume that the liquid bath remains in contact with the solid even in cases with $\bar{h}_s > 0$. On the other hand, net expansion ($\bar{h}_s^\infty$ negative) generally corresponds to relatively large values of ϕ_0. For the intermediate values of ϕ_0, details of other parameters values determines the nature of the final configuration. This suggest that materials with relatively high porosity tend to shrink while those with sufficiently low porosity tend to expand.

21
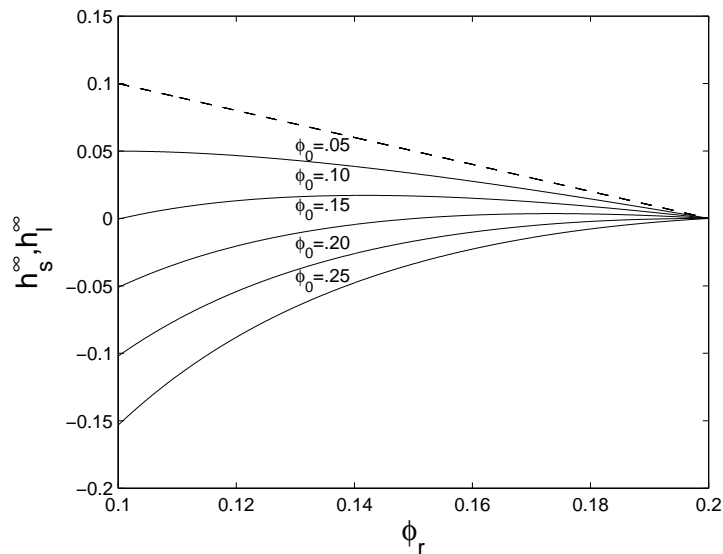
Figure 2.5: This plot shows $\bar{h}_s^\infty$ and $\bar{h}_\ell^\infty$ versus ϕ_r. The dashed line shows $\bar{h}_\ell^\infty$ and the solid lines show $\bar{h}_s^\infty$ for different ϕ_0 values. We have used $\rho = 0.1$ and $\phi_\ell^* = 0.20$.

Figure 6 shows the interface positions $(\bar{h}_s, \bar{h}_\ell)$ as a function of time for a particular choice of parameter values for which $\bar{h}_s^\infty = 0$. Initially, the porous solid material shrinks marked by positive h_s. Again, in order for $\bar{h}_s > 0$ to be physically realistic, we assume that the liquid bath remains in contact with the solid for all times. The overall behavior is that fluid rises to an equilibrium height and the wet solid interface rises initially but then returns to $\bar{z} = 0$ (no net deformation). However, as we show in the next plot there is local compression (relative to ϕ_0) near the bottom of the wet material and local expansion (relative to ϕ_0) near the top of the wet material. The opposite trend to that shown in figure 6 can also be observed where initially the porous material expands ($h_s < 0$) before the solid interface position returns to $\bar{z} = 0$.

Figure 7 shows a plot of solid volume fraction ϕ as a function of $\bar{z}$ for both steady state and unsteady cases. Good agreement between the numerical and steady state solution is found. Both are compared with a constant solution ϕ_0 indicated by dashed line. In this plot we have used a special value of ϕ_0 such that $\bar{h}_s^\infty = 0$. When $\phi > \phi_0$ the solid material is in a state of relative compression. When $\phi < \phi_0$ the solid material is in a state of relative

22
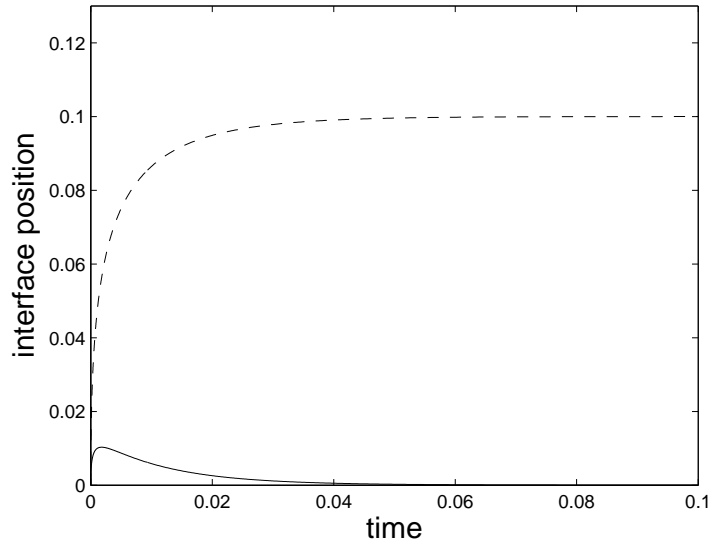
Figure 2.6: This plot shows the interface positions ($\bar{h}_\ell$ dashed line and $\bar{h}_s$ solid line) as a function of time for a special set of parameters that results in $\bar{h}_s^\infty = 0$. In particular we have used $\rho = 0.1$, $\phi_r=0.10$, $\phi_0 = 0.0995$ and $\phi_\ell^* = 0.20$.
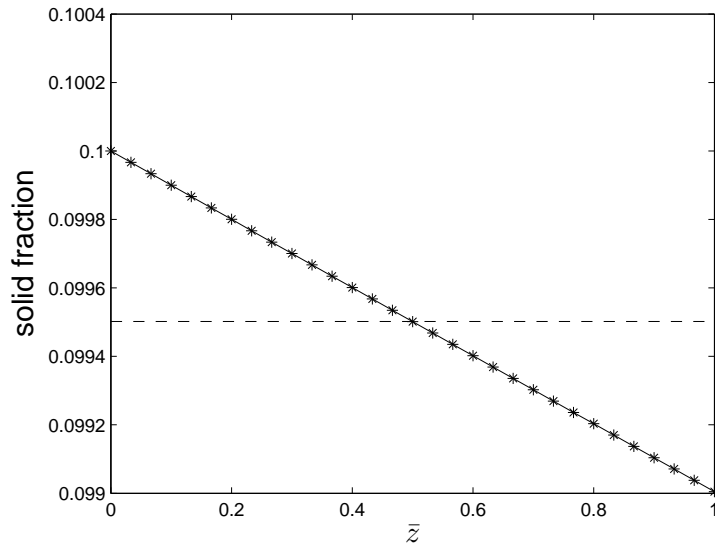
Figure 2.7: This plot shows solid fraction versus $\bar{z}$ for the long–time state associated with the previous figure. The solid line denotes the unsteady $\phi(\bar{z}, \bar{t})$ for $t \to \infty$ and $*$ denotes the steady ϕ solution. The dashed line denotes $\phi = \phi_0$ as reference. In these calculations, $\phi_0 = 0.0995$, $\phi_r = 0.10$, $\phi_\ell^* = 0.20$ and $\rho = 0.1$ which imply $\bar{h}_s^\infty = 0$.

expansion. When $\rho > 0$, the local expansion ($\phi < \phi_0$) occurs near the top while the local compression ($\phi > \phi_0$) occurs near the bottom. Note in this case there is local deformation as described but no net deformation (i.e. $h_s^\infty = 0$). This behaviour is in fact true in general, as can be seen from a derivative of the equilibrium solid fraction

$$\frac{d\phi}{d\bar{z}} = -\rho\phi_r(\bar{h}_\ell^\infty - \bar{h}_s^\infty)e^{\rho(\bar{h}_s^\infty - \bar{h}_\ell^\infty)\bar{z}} \qquad (2.56)$$

from equation (2.42). That is, when $\rho > 0$ the solid fraction decreases with increasing vertical position. The opposite trend occurs when $\rho < 0$; namely, the solid fraction increases with increasing vertical position. Finally, when $\rho = 0$ this equation shows that the equilibrium solid fraction is unifrom throughout the solid, with value $\phi = \phi_r$. Physically, when $\rho_s > \rho_\ell$ the solid material tends to preferentially accumulate near the bottom and when $\rho_\ell > \rho_s$ liquid tends to preferentially accumulate near the bottom.
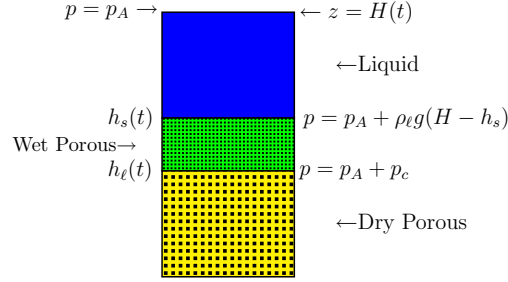
Figure 2.8: This figure shows the one–dimensional drainage configuration.

2.6 Drainage into a Deformable Porous Material

In the previous problem capillarity drove fluid flow in opposition to gravity. In this section we consider the opposite scenario in which capillary and gravational forces act in the same direction. In this setting, at time $t = 0$ we consider a finite amount of liquid with thickness H_0 in contact with the deformable porous material. The pressure at $z = H(t)$ is atmospheric pressure. The initial contact position of the liquid and porous material is defined by $z = 0$. For time $t > 0$ the liquid starts penetrating into the porous material. The upper interface of the porous material after deformation is defined by $z = h_s(t)$ and lower interface formed due to liquid penetration is defined by $z = h_\ell(t)$ as shown in figure 2.8. The governing equations (2.17)–(2.20) are the same as before in the wet region. Similarly, after combining equations (2.17), (2.23) and (2.24) we get the same PDE for ϕ (2.25) on $h_\ell(t) < z < h_s(t)$.

The boundary conditions applied at the liquid-wet material interface $z = h_s(t)$ are

$$w_s\left(h_s^-, t\right) = \frac{\partial h_s}{\partial t}, \tag{2.57}$$

$$p\left(h_s^-, t\right) = p_A - \rho_\ell g(h_s(t) - H(t)), \tag{2.58}$$

$$\sigma\left(h_s^-, t\right) = 0. \tag{2.59}$$

25

Here we have neglected inertial effects in the liquid region to get the hydrostatic pressure condition (2.58).

The boundary conditions applied at the wet material-dry material interface $z = h_\ell(t)$ are

$$w_\ell\left(h_\ell^+, t\right) = \frac{\partial h_\ell}{\partial t}, \tag{2.60}$$

$$p\left(h_\ell^+, t\right) = p_A + p_c. \tag{2.61}$$

We introduce the same dimensionless quantities as before to non-dimensionalize (2.25) on $h_\ell(t) < z < h_s(t)$ except that here we take

$$\bar{z} = \frac{z - h_\ell(t)}{h_s(t) - h_\ell(t)}. \tag{2.62}$$

The dimensionless PDE for ϕ can be written as

$$\frac{\partial \phi}{\partial \bar{t}} + \left[\frac{(\bar{z} - 1)}{(\bar{h}_s - \bar{h}_\ell)}\frac{d\bar{h}_\ell}{d\bar{t}} - \frac{\bar{z}}{(\bar{h}_s - \bar{h}_\ell)}\frac{d\bar{h}_s}{d\bar{t}}\right]\frac{\partial \phi}{\partial \bar{z}} + \frac{\bar{c}(\bar{t})}{(\bar{h}_s - \bar{h}_\ell)}\frac{\partial \phi}{\partial \bar{z}} =$$
$$\frac{1}{(\bar{h}_s - \bar{h}_\ell)^2}\frac{\partial^2 \phi}{\partial \bar{z}^2} + \frac{\rho}{(\bar{h}_s - \bar{h}_\ell)}\frac{\partial \phi}{\partial \bar{z}}, \tag{2.63}$$

where the function $c(\bar{t})$ is given by

$$\bar{c}(\bar{t}) = \frac{1 - \phi_0}{\phi_0}\left[\frac{1}{(1 - \phi)(\bar{h}_s - \bar{h}_\ell)}\frac{\partial \phi}{\partial \bar{z}} + \frac{\rho\phi}{(1 - \phi)}\right]\bigg|_{\bar{z}=0}. \tag{2.64}$$

The PDE (2.63) is subject to the boundary conditions

$$\phi = \phi_r, \qquad \text{at} \qquad \bar{z} = 1, \tag{2.65}$$

$$\phi = \phi_\ell^* + \bar{H} - \bar{h}_s + (\bar{h}_s - \bar{h}_\ell)\int_0^1 (\rho\phi + 1)d\bar{z} \qquad \text{at} \qquad \bar{z} = 0. \tag{2.66}$$

26

Note if $g = 0$, condition (2.66) reduces to $\phi = \phi_\ell^*$. The boundary condition (2.66) is obtained by integrating (2.24) and applying the pressure boundary conditions (2.58) and (2.61). The liquid height $\bar{H}(t)$ follows from conservation of liquid

$$\bar{H}(t) = \bar{H}_0 + \bar{h}_s - (\bar{h}_s - \bar{h}_\ell) \int_0^1 (1 - \phi) d\bar{z}, \tag{2.67}$$

were $\bar{H}_0$ is the dimensionless initial height of the liquid region.

The dimensionless interface positions satisfy the ODEs

$$\frac{d\bar{h}_s}{d\bar{t}} = \bar{c}(\bar{t}) - \left[\frac{1}{\phi(\bar{h}_s - \bar{h}_\ell)} \frac{\partial \phi}{\partial \bar{z}} + \rho \right]\bigg|_{\bar{z}=1}, \tag{2.68}$$

$$\frac{d\bar{h}_\ell}{d\bar{t}} = \bar{c}(\bar{t}) + \left[\frac{1}{(1 - \phi)(\bar{h}_s - \bar{h}_\ell)} \frac{\partial \phi}{\partial \bar{z}} + \frac{\rho\phi}{(1 - \phi)} \right]\bigg|_{\bar{z}=0}. \tag{2.69}$$

The initial conditions for the interface positions are

$$\bar{h}_\ell(\bar{t} = 0) = 0, \qquad \bar{h}_s(\bar{t} = 0) = 0, \qquad \text{and} \quad \bar{H}(\bar{t} = 0) = \bar{H}_0. \tag{2.70}$$

We will use the same solution technique to solve the equations (2.63)–(2.70).

Figure 9 shows interface positions $\bar{h}_s, \bar{h}_\ell$ and $\bar{H}$ as a function of time. A finite amount of liquid is supplied whose thickness is shown by $\bar{H}(t)$ in the plot. Note, that in the absence of gravity, the solution does not depend on ρ. Here, both curves $\bar{h}_s(t)$ and $\bar{h}_\ell(t)$ follow the similarity solution of the case of the zero gravity capillary rise problem until the fluid layer is completely drained into the porous material when $\bar{h}_s = \bar{H}$. For the nonzero gravity case, both curves follow the similarity solution initially but then depart from this trend until again the liquid layer has completely drained. We define a drainage time as the time at which all the liquid is drained into the porous material $\bar{t} = t^*$ $(\bar{h}_s(t^*) = \bar{H}(t^*))$. This drainage time is faster for the non–zero gravity case as compared to the zero gravity case.
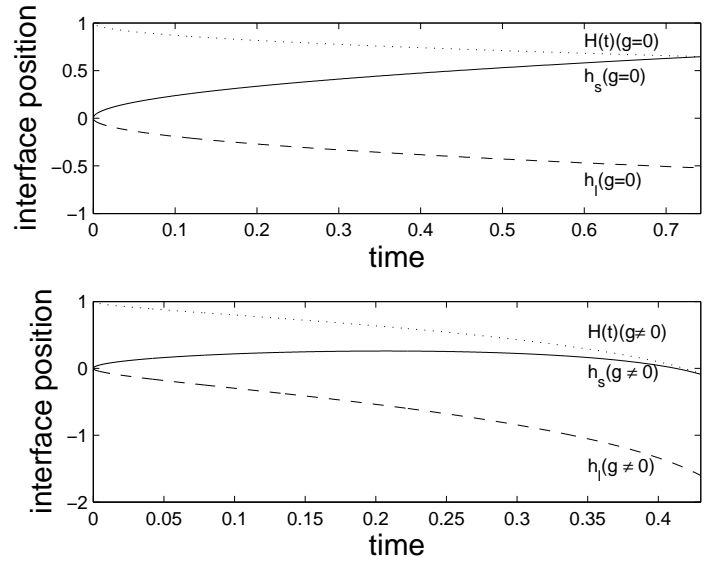
Figure 2.9: This plot shows the evolution of the interface positions $\bar{h}_s$, $\bar{h}_\ell$ and $\bar{H}(t)$ for $g = 0$ and $g \neq 0$ when a finite amount of liquid penetrates into the deformable porous material. In this plot we have used $\phi_\ell^* = 0.2$, $\phi_r = 0.1$, $\phi_0 = 0.33$ and $\rho = 0.1$.
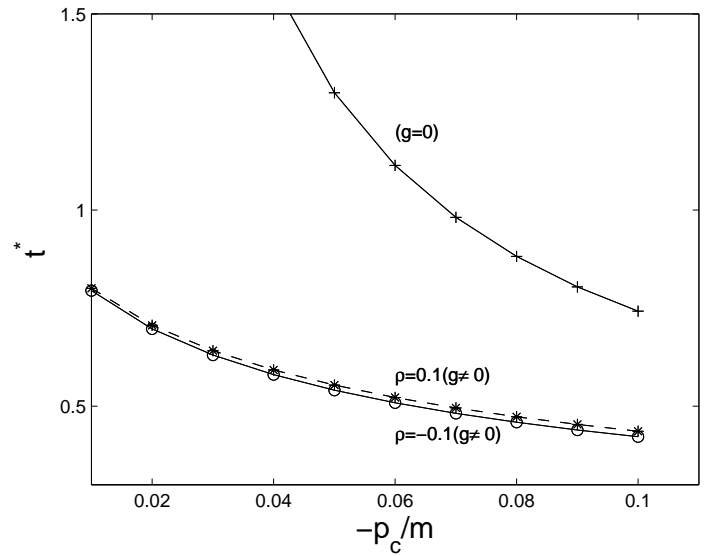
Figure 2.10: This is a plot of drainage time (t^*) versus dimensionless capillary pressure. We have used $\phi_r = 0.1$, and $\phi_0 = 0.33$. The upper curve shown by $+$ is for the zero gravity case; here note that the $g = 0$ solution does not depend on ρ. For non–zero gravity, the curve with $*$ is for $\rho = 0.1$ and the curve with o is for $\rho = -0.1$

Figure 10 shows the drainage time (t^*) as a function of dimensionless capillary pressure $-p_c/m$. As capillary suction is increased the drainage time t^* decreases. When gravity is present, this quantity depends on the density ratio ρ. In particular, the drainage time is larger when $\rho > 0$ (solid more dense than liquid) as compared to when $\rho < 0$ (solid less dense than liquid). In the absence of gravity increasing the capillary suction also decreases t^*. For the zero gravity case, the drainage time is independent of ρ.

2.7 Conclusion

We have considered a one dimensional model of capillary flow into a deformable porous material in the presence of gravity. This model is based on the work of Barry and Aldis [6], Preziosi et al [57], Anderson [3] and is similar to other models of flow in deformable materials [60]. Our new contribution is a set of analytical and numerical results that detail the effects of gravity and capillarity on the material deformation in these systems. Our capillary–rise results of deformable porous materials are analogous to the classical Washburn results for capillary rise in rigid porous materials.

In the presence of gravity initially both interface positions, separating the liquid bath and wet porous material and dry porous material and wet porous material follow the square root in time behavior as in the zero gravity case. However, in contrast to the zero gravity case where no steady state exists, the interface positions ultimately reach to steady state values $\bar{h}_s^\infty$ and $\bar{h}_\ell^\infty$. This fluid motion and solid deformation is driven by capillary suction; when capillary pressure is zero no fluid is imbibed into the material and consequently no deformation occurs.

We have quantified the deformation and imbibition dependence on fundamental quantities such as the strength of capillary suction and the solid-liquid density ratio. Deformation on both local and global scales has been assessed. Increased capillary pressure leads to increased net deformation. Also the net deformation of the solid increases with increasing $\rho = (\rho_s/\rho_\ell - 1)$. The deformation within the sponge has also been assessed. In particular,

when the solid is more dense than the liquid we observe that there is local expansion near the top and local compression near the bottom. An opposite trend is observed when the solid is less dense than the liquid, where there is local expansion near bottom and local compression near the top.

In our capillary rise configuration, the equilibrium rise height of liquid is the same for both rigid and deformable geometries assuming the same capillary pressure in both cases. This is also related to our assumption that the pressure is fixed at a fixed location $\bar{z} = 0$ rather than at the bottom of deforming solid. Therefore the noted increase in net deformation is measured by the position of the wet sponge-liquid interface.

We have also examined the case in which capillary and gravitational forces act in the same direction. Here we measure the time required for a finite volume of fluid to penetrate into the deformable material. It is observed that drainage of liquid is faster for the non–zero gravity case as opposed to when gravity is absent. We have also observed that drainage time decreases as capillary suction is increased. When gravity is present we find that when the solid is more dense than the liquid, the drainage time is slower than when the solid is less dense than the liquid.

These capillary and gravity interactions in one–dimensional deformable porous materials highlight a number of interesting phenomena that suggest further analysis of models in higher dimensions as well as experiments.

Chapter 3: Capillary Rise of non–Newtonian Fluid into Deformable Porous Materials

3.1 Introduction

The phenomena of capillary rise and fluid flow through porous materials has been long studied by various researchers. In the past, both Newtonian and non–Newtonian fluid models have been used to formulate the problems of fluid flow through rigid porous materials whereas the subject of non–Newtonian fluid flow through deformable porous materials has not received that much attention. Capillary rise dynamics are present in industrial as well as biological settings such as the pharmaceutical industry [16; 31; 65], textile manufacturing [55], paper inkjet printing [18; 27], medical science [6; 7; 8; 33; 34; 35; 36; 37; 38], oil recovery [52; 53] and geological flows [61].

In this work we study a model of capillary rise of a non–Newtonian fluid through a deformable porous material that extends previous work on non–Newtonian flows in rigid materials as well as Newtonian flows in deformable porous materials. One of the early major results on capillary rise dynamics into porous materials was the pioneering work of Wasburn [64]. According to this classical model, in the absence of gravity effects, the volume of liquid that is imbibed by the porous material during time t is proportional to $\sqrt{t}$, whereas when capillarity competes against gravity the liquid penetrates to a finite height. Recent experimental and theoretical models on capillary rise of water into packings of glass beads [23; 46; 66] have validated Washburn's early time dynamics $t^{1/2}$ whereas for long time the data deviate from equilibrium predictions. In particular for these later time experimental observations capillary rise dynamics follows a different power law.

Recently, Siddique et al. [59] (see also chapter 2) have studied a model of capillary rise

into deformable porous materials for Newtonian fluids. In this work they have performed experiments on the capillary rise of water into a deformable sponge and compared the liquid interface height and solid deformation depth with their theoretical predictions. Their model is an analog of the Washburn model where the deformation in the porous material is also taken into account. Their modeling approach follows closely to models that take into account both the capillary rise dynamics and material deformation in industrial [3; 57; 60] as well as biological [6; 7; 8] contexts. According to their theoretical model, initially in the presence of gravity effects both liquid and solid interface positions follow a square root in time behavior whereas for long time the interface positions reach to equilibrium heights. According to their experiments, the early time dynamics of the capillary rise and material deformation follow the $t^{1/2}$ dynamics as predicted by capillary rise theory but for long times their experimental results, much like those for rigid porous materials [23; 46; 66], show a power law dynamics different than the equilibrium predictions.

In the above discussion we have briefly described classical and recent work in both rigid and deformable porous material contexts for Newtonian fluids. Now we turn our attention towards non–Newtonian fluid flow through rigid porous materials. There are a variety of non–Newtonian fluids which we encounter in our everyday life such as crude oil, honey, toothpaste, paint and blood. There are many types of non–Newtonian models: Power law, viscoelastic fluids etc. [14]. For these non–linear and non–Newtonian flows the widely used Darcy's law is not valid; a modified version accounting for these effects is required. In the case of a power law fluid the ratio of permeability to viscosity, which is the usual proportionality factor between the fluid velocity and the pressure gradient in the Newtonian case, is modified to account for the non–Newtonian viscosity. Typically one assumes that the permeability relation is the same for Newtonian and non–Newtonian cases. However, the relation between velocity and pressure gradient is no longer linear. We provide more specific details in the next sections.

Christopher and Middleman [19] developed a modified Darcy equation referred to there as a modified Blake–Kozeny equation for a power law fluid with laminar flow through

packed tubes. Their capillary model was tested experimentally when a diluted polymer solution flowed through a tube packed with spherical particles. The results obtained in this study were then compared with that of Sadowski [58]. The major difference between the Christopher and Middleman and Sadowski [58] models is that Sadowski has used the Ellis model to study the non–Newtonian fluid flow through packed beds of glass beads. Sadowski also used the same formula for permeability but with different constant prefactors (see also Bear [9] and Kemblowski [43]).

Hayes et al. [32] used the volume averaging approach to model the flow of a power–law fluid to examine the velocity and pressure drop through a porous bed packed with spherical particles. In their article they have reviewed the modifications and developments in Darcy's law and intrinsic permeability for non–Newtonian fluids examined by different authors [19; 43; 52].

Many authors [1; 19; 62] have used an approach in which spherical particles are approximated as a bundle–of–tubes to model the flow of non–Newtonian fluids in porous media. The use of this approximation to model the non–Newtonian flow in porous media is limited due to the fact that typical porous media are not capillary tubes but rather a complex network of interconnected throats. In recent work [5], network based modeling has been used to model the flow of shear–thinning fluids in packed beds in order to study the effects of fluid rheology and bed morphology on flow. According to this approach, the porous medium is approximated as an interconnected networks of pores and pore throats.

Many industrial as well as biological processes mentioned earlier involve the flow of non–Newtonian fluid through porous materials. A large amount of work [3; 6; 7; 8; 57; 60] has been dedicated to study the Newtonian fluid flow through deformable porous materials. The governing mechanics of these flows is coupled to the deformation of the porous material. The material deformation caused by the fluid flow in turn affects the fluid flow through the porous material. There is a need for such models that can take into account both non–Newtonian fluid flow and material deformation. In this work we address the particular situation of one dimensional capillary rise of a non–Newtonian fluid through a deformable porous material.

This provides a setting in which one can gain insight into capillary rise phenomena as well as explore features of non–Newtonian fluids in deformable porous materials. We do so by combining ideas of capillary rise of a Newtonian fluid into deformable porous materials and non–Newtonian fluid flow into rigid porous materials.

The chapter is outlined as follows. In section two, we derive the general system of equations using mixture theory. In section three, we discuss the modeling and solution of non–Newtonian fluid flow into rigid porous materials. In section four, we model the one–dimensional capillary rise of a power law fluid into a deformable porous materials. Finally, in section five, we present the results and discussion.

3.2 The Model

We study the problem of capillary rise of a non–Newtonian fluid into a deformable porous material. We model the deformable porous material using mixture theory. Detailed descriptions of mixture theory can be found in [6; 7; 8; 15; 36] and in chapter 2.

The model is stated in terms of mass and momentum balances for both solid and liquid phases. For the case of constant true intrinsic densities of solid ρ_s and liquid ρ_ℓ respectively, the conservation of mass of each constituent is expressed by

$$\frac{\partial \phi}{\partial t} + \nabla \cdot (\phi \vec{w}_s) = 0, \tag{3.1}$$

$$-\frac{\partial \phi}{\partial t} + \nabla \cdot [(1 - \phi)\vec{w}_\ell] = 0, \tag{3.2}$$

where ϕ is the solid volume fraction and $\vec{w}_s$ and $\vec{w}_\ell$ are the velocities of solid and liquid constituents respectively. The momentum balances for liquid and solid constituents are

$$\rho_s \phi \left(\frac{\partial \vec{w}_s}{\partial t} + \vec{w}_s \cdot \nabla \vec{w}_s \right) = \nabla \cdot \mathbf{T}_s + \phi \rho_s \vec{g} + \vec{\pi}_s, \tag{3.3}$$

34

$$\rho_\ell(1-\phi)\left(\frac{\partial \vec{w}_\ell}{\partial t} + \vec{w}_\ell \cdot \nabla \vec{w}_\ell\right) = \nabla \cdot \mathbf{T}_\ell + \rho_\ell(1-\phi)\vec{g} + \vec{\pi}_\ell, \qquad (3.4)$$

where $\mathbf{T}_s$ and $\mathbf{T}_\ell$ are stress tensors for solid and liquid phases, $\vec{g}$ is gravity and $\vec{\pi}_s$ and $\vec{\pi}_\ell$ are drag forces.

We will neglect the inertial terms in equations (3.3) and (3.4) due to the assumption that the fluid velocities and deformation rates are small. According to Newton's third law the force on the solid by the liquid is opposite to that on the liquid by the solid $\vec{\pi}_\ell = -\vec{\pi}_s$. We follow Barry and Aldis [6] and write the stress tensors as

$$\mathbf{T}_s = -\phi p\mathbf{I} + \boldsymbol{\sigma}_s, \qquad \boldsymbol{T}_\ell = -(1-\phi)p\mathbf{I} + \boldsymbol{\sigma}_\ell, \qquad (3.5)$$

where $\boldsymbol{\sigma}_s$ and $\boldsymbol{\sigma}_\ell$ are solid and liquid stresses, p is the pressure and $\mathbf{I}$ is the identity tensor. Here we neglect the viscous stress $\boldsymbol{\sigma}_\ell$ and we take $\boldsymbol{\sigma}_s = \boldsymbol{\sigma}$, where $\boldsymbol{\sigma}$ is to be specified below. In usual power law fluid modeling the non–Newtonian effects enter through viscous stress $\boldsymbol{\sigma}_\ell$ whereas in the present model under the above assumptions the non–Newtonian effects enter through the drag forces and those are the terms we focus on here.

The appropriate details for drag force terms for rigid, deformable, Newtonian and non–Newtonian fluids will be included in the later sections. In the section below we will discuss the capillary rise of a non–Newtonian liquid into a one dimensional rigid porous material in the presence and absence of gravity effects.

3.3   One dimensional capillary rise of power law fluid into rigid porous material

In this section, we will discuss one dimensional capillary rise of a power law fluid into a rigid porous material. Here we assume that the upper end of the initially dry rigid porous material is fixed. At time $t = 0$, the contact position of the porous material and liquid bath is at $z = 0$. We also assume that the capillary rise of fluid occurs from an infinite bath of fluid whose upper surface at $z = 0$ remains open to atmospheric pressure (i.e. $p = p_A$ at

$z = 0$ for all time) and the pressure in the fluid bath is hydrostatic i.e.($p = p_A - \rho_\ell g h_s$ at $z = h_\ell$). For $t > 0$, liquid starts rising into the porous material due to the capillary suction in the pore space of the porous material assuming the capillary pressure $p_c < 0$. In this setting $z = h_\ell(t)$ denotes the liquid interface. In this case we also assume that solid constituents are not moving ($w_s = 0$) and introduce the drag force in a one dimensional setting for rigid porous material as $\pi_\ell = -\frac{(1-\phi)^2 \mu_{eff}}{K(\phi)} |w_\ell|^{n-1} w_\ell$, here n is power law index, μ_{eff} is an effective viscosity and $K(\phi)$ is permeability function. In this relation for drag force if we set $n = 1$, this relation reduces to one used for the Newtonian fluid case. For $n < 1$ and $n > 1$ one gets the shear thinning and shear thickening fluid cases respectively.

After combining the above assumptions with (3.1), conservation of mass for the rigid porous materials is written as

$$\frac{\partial w_\ell}{\partial z} = 0,$$

(3.6)

and (3.4) momentum balance for the power law fluid can be written as

$$w_\ell = \left[-\frac{K(\phi)}{(1 - \phi)\mu_{eff}} \left(\frac{\partial p}{\partial z} + \rho_\ell g \right) \right]^{1/n}.$$

(3.7)

In equation (3.7) we assume the capillary pressure p_c to be sufficiently negative that implies $\left(\frac{\partial p}{\partial z} + \rho_\ell g \right) < 0$ so that $w_\ell > 0$. In this case the only unknowns are the velocity of the liquid w_ℓ, the liquid interface position h_ℓ and the pressure p. Equation (3.7) is the modified Darcy's equation for flow in porous medium for power–law fluid proposed by Bird et al. [14]. Bird et al. have developed the following formulas for permeability of a bed of particles of diameter d and solid volume fraction ϕ

$$K(\phi) = W(\phi)d^2, \qquad W(\phi) = \frac{(1 - \phi)^3}{150\phi^2},$$

(3.8)

36

with μ_{eff} for a power law fluid

$$\mu_{eff} = \mu^* Y(\phi, n) d^{1-n}, \tag{3.9}$$

where

$$Y(\phi, n) = \left[\frac{25}{6} \left(\frac{3n+1}{n(1-\phi)} \right)^n \left(\frac{3(1-\phi)}{50} \right) \left(\frac{1-\phi}{\phi} \right)^{1-n} \right]. \tag{3.10}$$

Setting $n = 1$ in relation (3.9) we recover the Newtonian case where μ^* would be the standard Newtonian viscosity. When $n \neq 1$, μ^* is called the power law consistency index and has a units of Pa s^n.

Substituting (3.7) in (3.6) and using the pressure boundary conditions $p(z = 0) = p_A$ and $p(z = h_\ell) = p_A + p_c$ yields the following solution for pressure

$$p(z) = \frac{p_c}{h_\ell} z + p_A. \tag{3.11}$$

When gravity effects are not present equation (3.7) after using boundary condition $w_\ell(z = h_\ell, t) = \frac{dh_\ell}{dt}$ admits an analytical solution

$$h_\ell = \left[\frac{K(\phi)|p_c|}{(1-\phi)\mu^*} \left(\frac{n+1}{n} t \right)^n \right]^{\frac{1}{n+1}}. \tag{3.12}$$

The above formula can be written in dimensionless form as follows

$$\bar{h}_\ell = \left[Da^{\frac{n+1}{2n}} \xi \left(\frac{W(\phi)}{Y(\phi, n)} \right)^{\frac{1}{n}} \bar{t} \right]^{\frac{n}{n+1}}, \tag{3.13}$$

where $\xi = \frac{\mu}{\mu^{*\frac{1}{n}}} |p_c|^{\frac{1-n}{n}}$ is a dimensionless quantity. We have picked the choices of non–dimensional quantities in such a way that the length scale $L = \frac{|p_c|}{\rho_\ell g}$ and time scale $T =$

$\frac{\mu}{|p_c|}$ are independent of n values. An additional quantity that appears as result of non–dimensionalization is Darcy's number $Da = \frac{d^2}{L^2}$. Note that the length scale L depends on g that we use when gravity effects are included in the model. The formula (3.12) and (3.13) obviously depends on n. Additionally, the consistency index μ^* is typically determined empirically for different power law fluids and is therefore also n–dependent. The permeability function $K(\phi)$ depends on ϕ and the typical pore scale radius d. Here we have used the specific form for capillary pressure $|p_c| = \frac{\gamma cos\theta}{d}$, where γ is surface tension assumed to be constant for all non–Newtonian cases and θ is the wetting angle which in our case we assume to $\theta = 0°$. In the case of a rigid porous material we have assumed the solid volume fraction $\phi = \phi_0$ to be constant.

It is important to understand the dynamics of different power law fluids. We will investigate this by observing the evolution of interface positions of these fluids in different time regimes. In table 3.1, we have listed consistency index μ^* and power law index values for test fluids $V_N, V2, V4$ and $V8$ where V_N represent the Newtonian case and $V2, V4$ and $V8$ represent the non–Newtonian $n < 1$ cases. For different values of n the formula (3.13) on loglog scales generates lines with different slopes. Table 3.1 also contains the intersection times between these lines; these lines intersect each other at some time that leads us to the understanding of change in the dynamics of Newtonian and non–Newtonian fluids in different time regime. The intersection time t^* for these lines is given by

$$t^* = \left[\frac{\left(\frac{n_2+1}{n_2}\right)^{\frac{n_2}{n_2+1}} \left(\frac{K(\phi)p_c}{(1-\phi_0)\mu_2^*}\right)^{\frac{1}{n_2+1}}}{\left(\frac{n_1+1}{n_1}\right)^{\frac{n_1}{n_1+1}} \left(\frac{K(\phi)p_c}{(1-\phi_0)\mu_1^*}\right)^{\frac{1}{n_1+1}}} \right]^{\frac{(n_1+1)(n_2+1)}{(n_1-n_2)}} .$$

Here n_i and μ_i^* are the power law index and consistency index values respectively for fluids $i \in \{1, 2\}$. One can see from table 3.1, that some of the intersection times are very small and other very large. In figure 3.1 we have shown one of the intersection time.
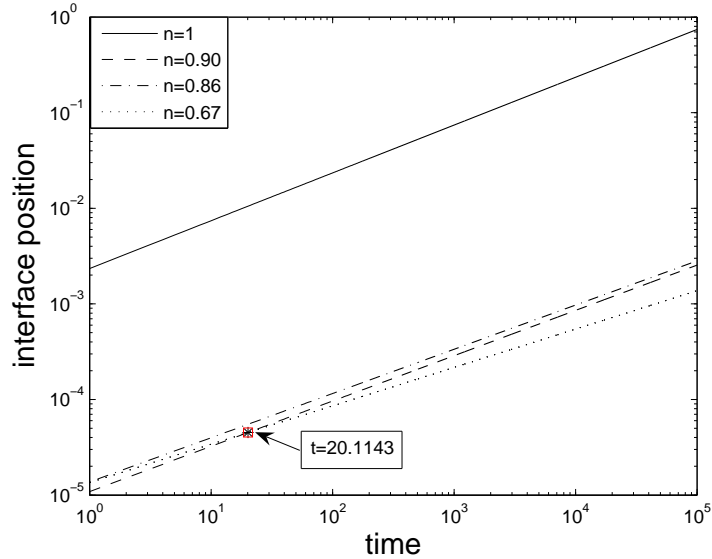
Figure 3.1: This plot shows the evolution of interface positions h_ℓ versus time t for Newtonian and non–Newtonian fluid in the absence of gravity effects. Here we have used $Da = 0.01$, $d = 0.0001$ m, $\phi_0 = 0.33$ and surface tension 63.57×10^{-3}N/m.

Table 3.1: This table shows the intersection time t^* for different fluids. Consistency index μ^* and power law index n values used in this study are from [50]. Where V_N represents the Newtonian fluid and V2, V4, and V8 represent the non–Newtonian test fluids.

Test fluid	$\mu^*(kPas^n)$	n	$t^*_{V_N}$	t^*_{V2}	t^*_{V4}	t^*_{V8}
V_N	10^{-3}	1	–	2.1645×10^{-89}	4.8831×10^{-60}	2.1913×10^{-23}
V2	0.095	0.90	–	–	8.6139×10^8	20.1143
V4	0.082	0.86	–	–	–	0.7786
V8	0.340	0.67	–	–	–	–

39

Figure 3.1 shows the evolution of interface position $\bar{h}_\ell$ with respect to time $\bar{t}$ for Newtonian $n = 1$ and shear thinning $n < 1$ fluids. The consistency index values used in this study are for a shear thinning fluid given in [50]. These interface position predictions depend on the power law index n, capillary pressure p_c, solid volume fraction ϕ, Darcy's number Da and consistency index μ^*. The intersection times given in table 3.1 range from very small values to very large values. It is difficult to show the intersection time for all of these lines. For real early times the ordering (from bottom to the top not actually visible in Figure 3.1) of these lines is from larger values of power law index n to small values whereas for large enough time the ordering (from bottom to the top) of power law index n is from small to large values. This tells us that the non–Newtonian fluid is faster initially and vise versa. The ordering of these curves tells us which fluid moves faster in which time regime. For early times, capillary rise of Newtonian fluid is faster than the non–Newtonian fluid but this trend is opposite for larger times. This change in trend varies for different combination of Newtonian and non–Newtonian fluids. In Figure 3.1 an intersection time between $n = 0.67$ and $n = 0.90$ with asterisk in a red square is shown. This intersection time in the actual time units $t = 31.64\,\mathrm{sec}$ (i.e. T=1.5 sec).

When gravity effects are present equation (3.7) yields an ordinary differential equation

$$\frac{dh_\ell}{dt} = \left[\frac{K(\phi)}{(1 - \phi)\mu_{eff}} \right]^{\frac{1}{n}} \left(\frac{|p_c|}{h_\ell} - \rho_\ell g \right)^{1/n}. \tag{3.14}$$

The above ordinary differential equation is solved numerically subject to appropriate initial conditions.

In Figure 3.2 the plot of interface position h_ℓ with respect to time t for Newtonian and shear thinning fluids is shown. When gravity effects are present the fluid reaches to an equilibrium height. As shown in Figure 3.2 the Newtonian fluid reaches to an equilibrium height before the non–Newtonian fluid. Note that the ordering (from bottom to the top in Figure 3.2) of lines in this case are also from smaller values of power law index n to the larger
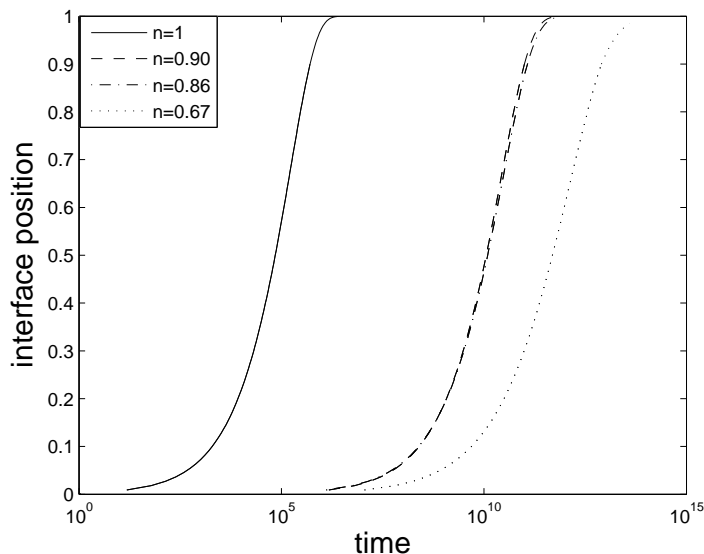
Figure 3.2: This plot shows the evolution of interface positions h_ℓ versus time t for Newtonian and non–Newtonian fluid in the presence of gravity effects. Here we have used $Da = 0.01$, $d = 0.0001$ m, $\phi_0 = 0.33$ and surface tension 63.57×10^{-3}N/m

values of power law index n. Again we show results in terms of dimensionless variables with $L = \frac{|p_c|}{\rho_\ell g}$ and $T = \frac{\mu}{|p_c|}$. These length and time scales are related through capillary pressure that depends on particle diameter d. When the Darcy number Da or capillary pressure p_c is increased the imbibition of the fluid increases and when the Darcy number Da or capillary pressure p_c is decreased the imbibition of the fluid decreases. Another parameter that effects the imbibition of the fluid is consistency index μ^*. If μ^* is increased, imbibition of the fluid into the porous material decreases and if μ^* is decreased, imbibition of the fluid increases. One can understand this by noting that increasing μ^* increases the friction force, which slows the dynamics. In Figure 3.3 we have shown the effect of increase (imbibition decreases, shown by dashed dotted line) and decrease (imbibition increases, shown by solid line) of power law consistency index μ^* by a factor of 10. Note that the curve shown by dashed line is with the same consistency index value used to generate Figure 3.2.

41
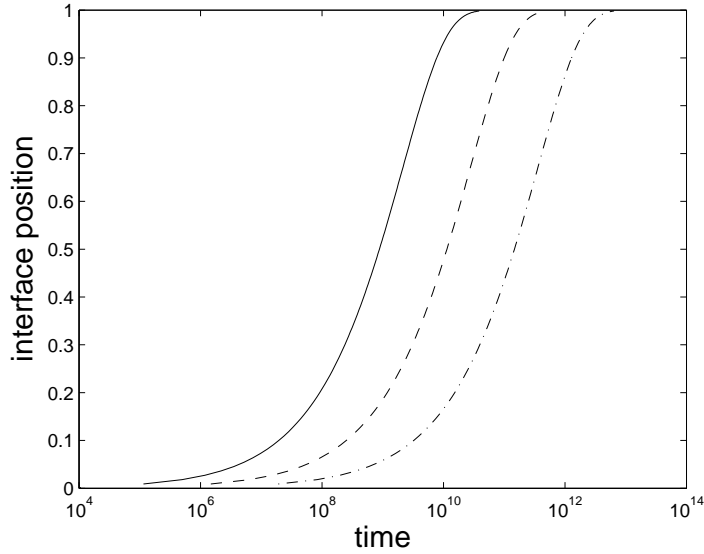
Figure 3.3: This plot shows the evolution of interface positions $\bar{h}_\ell$ versus time $\bar{t}$ for non–Newtonian fluid for same power law index $n = 0.90$ and $\mu^* = 9.5, 95, 950$ Pa s^n from left to right in the presence of gravity effects. Here we have used $Da = 0.01$, $d = 0.0001$ m, $\phi_0 = 0.33$ and surface tension 63.57×10^{-3}N/m.

3.4 One-dimensional capillary rise of a shear thinning liquid into a deformable porous material

In this section we extend the ideas and results of the previous sections to deformable porous materials. Specifically, we focus on a one dimensional deformation of a deformable sponge-like material in contact with a liquid. This is the same geometry considered in [59] and in chapter 2. For clarity we briefly we describe this configuration here. We assume that the upper end of the deformable material is fixed and the porous material is initially dry. At time $t = 0$, the contact position of the deformable material and liquid is defined by $z = 0$. It is assumed that the imbibition of fluid occurs from an infinite bath of fluid whose upper surface at $z = 0$ remains open to atmospheric pressure (i.e. $p = p_A$ at $z = 0$ for all time). The upper interface of the wet porous material region is defined by $z = h_\ell(t)$ and the lower interface formed after the deformation is defined by $z = h_s(t)$ as shown in figure 2.1 in chapter 2. We have assumed that the pressure in the fluid bath is hydrostatic which implies

42

that $p = p_A - \rho_\ell g h_s$ at $z = h_s(t)$. Initially the dry porous material has uniform solid fraction ϕ_0.

As a result of the above assumptions, the only remaining unknowns are those in the wet material and the boundary positions h_s and h_ℓ. The variables of interest in the wet region are the solid fraction ϕ, the vertical velocity component of the liquid phase w_ℓ, the vertical velocity component of solid phase w_s, the liquid pressure p and the stress in the solid $\boldsymbol{\sigma}$ where $\boldsymbol{\sigma} = \sigma(\phi)\boldsymbol{I}$ and $\sigma(\phi)$ is solid stress whose form we specify below. The drag force for the one dimensional deformable porous material case is defined as $\pi_\ell = -\pi_s = \frac{(1-\phi)^2 \mu_{eff}}{K(\phi)} |w_s - w_\ell|^{n-1}(w_s - w_\ell) - p\nabla\phi$. Setting $n = 1$ in this relation one can recover the relation used for Newtonian deformable porous material case [6; 59; 3; 2] and setting $w_s = 0$ and $\phi = \texttt{constant}$ one can yields rigid non–Newtonian case. For $n < 1$ and $n > 1$ this relation yields a drag force for shear thinning and shear thickening fluid cases. The set of equations (3.1)–(3.4) for the one dimensional material deformation reduces to

$$\frac{\partial \phi}{\partial t} + \frac{\partial}{\partial z}(\phi w_s) = 0, \tag{3.15}$$

$$\frac{\partial \phi}{\partial t} - \frac{\partial}{\partial z}[(1 - \phi)w_\ell] = 0, \tag{3.16}$$

$$(w_s - w_\ell)^n = -\frac{K(\phi)}{(1 - \phi)\mu_{eff}}\left(\frac{\partial p}{\partial z} + \rho_\ell g\right), \tag{3.17}$$

$$0 = -\frac{\partial p}{\partial z} + \frac{\partial \sigma}{\partial z} - g\left[\rho_s \phi + \rho_\ell(1 - \phi)\right], \tag{3.18}$$

where ρ_s and ρ_ℓ are the true intrinsic densities of solid and liquid respectively assumed to be constant. Note that equations (3.18) and (2.20) are same in both Newtonian and non–Newtonian cases which we will be using to compute one of the boundary condition for solid volume fraction after substituting the constitutive relation $\sigma = \sigma(\phi)$ in (3.18) in the presence of gravity effects.

Using the same procedure as in [59] and chapter 2 equations (3.15)–(3.18) can be reduced to a single partial differential equation for the solid fraction ϕ, as in [3; 59]

$$\frac{\partial \phi}{\partial t} + c(t)\frac{\partial \phi}{\partial z} = \frac{\partial}{\partial z}\left[-\frac{\phi^n K(\phi)(1-\phi)^{n-1}}{\mu}\left\{\sigma'(\phi)\frac{\partial \phi}{\partial z} - g(\rho_s - \rho_\ell)\phi\right\}\right]^{\frac{1}{n}}, \qquad (3.19)$$

on $h_s(t) < z < h_\ell(t)$.

The boundary conditions are the same as in the case of a Newtonian fluid. At liquid-wet material interface $z = h_s(t)$,

$$w_s\left(h_s^+, t\right) = \frac{\partial h_s}{\partial t}, \qquad (3.20)$$

$$p\left(h_s^+, t\right) = p_A - \rho_\ell g h_s(t), \qquad (3.21)$$

$$\sigma\left(h_s^+, t\right) = 0, \qquad (3.22)$$

where p_A is atmospheric pressure. The equations (3.20)–(3.22) are the kinematic conditions, hydrostatic pressure assumption in the liquid bath, and zero stress condition respectively.

At the wet material-dry material interface $z = h_\ell(t)$

$$w_\ell\left(h_\ell^-, t\right) = \frac{\partial h_\ell}{\partial t}, \qquad (3.23)$$

$$p\left(h_\ell^-, t\right) = p_A + p_c. \qquad (3.24)$$

Here (3.23) and (3.24) are kinematic and capillary pressure conditions respectively.

After some mathematical manipulation these boundary conditions (3.20,3.23) lead to ordinary differential equations for solid and liquid interfaces

$$\frac{\partial h_s}{\partial t} = c(t) - \left[-\frac{K(\phi)(1-\phi)^{n-1}}{\mu}\left(\sigma'(\phi)\frac{\partial \phi}{\partial z} - g(\rho_s - \rho_\ell)\phi\right)\bigg|_{h_s^+}\right]^{\frac{1}{n}}, \qquad (3.25)$$

$$\frac{\partial h_\ell}{\partial t} = c(t) + \left[-\frac{\phi^n K(\phi)}{\mu(1-\phi)} \left(\sigma'(\phi)\frac{\partial \phi}{\partial z} - g(\rho_s - \rho_\ell)\phi \right)\Big|_{h_\ell^-} \right]^{\frac{1}{n}}. \tag{3.26}$$

The function $c(t)$ is determined using the same procedure as in [59] and chapter 2

$$c(t) = \frac{(1-\phi_0)}{\phi_0} \left[-\frac{\phi^n K(\phi)}{\mu(1-\phi)} \left(\sigma'(\phi)\frac{\partial \phi}{\partial z} - g(\rho_s - \rho_\ell)\phi \right)\Big|_{h_\ell^-} \right]^{\frac{1}{n}}. \tag{3.27}$$

We use the following stress to local solid volume fraction relation $\sigma(\phi) = m(\phi_r - \phi)$, this choice is consistent with physically realistic trends (see ([3],[59]) for more details). Here we take $m > 0$ so that $\sigma'(\phi) = -m < 0$. Our assumption for the stress function σ is suitable for a one dimensional setting and Non–Newtonian fluid as the stress function is related to solid stress. For higher dimension one needs to modify the choice for σ that could take into account the effects of shear deformation.

Setting $n = 1$ in (3.25) (3.26) and (3.27), recovers the Newtonian case. In the next section we will discuss the solution methodology, when the gravity effects are not present.

3.5   Zero Gravity Case:

When gravity effects are not present the problem admits a similarity solution. Introducing the following similarity variable

$$\eta = \frac{z}{\left(\frac{n+1}{n}\right)(D^*t)^{\frac{n}{n+1}}}, \tag{3.28}$$

yields the following ODE

$$\left(-\frac{n}{n+1}\right)^{\frac{1}{n}} \eta\frac{d\phi}{d\eta} + \frac{1-\phi_0}{\phi_0} \left\{ \frac{W(\phi)\phi^n}{Y(\phi,n)(1-\phi)}\frac{d\phi}{d\eta}\Big|_{\lambda_\ell^-} \right\}^{\frac{1}{n}} \frac{d\phi}{d\eta} = \frac{d}{d\eta} \left\{ \frac{W(\phi)\phi^n(1-\phi)^{n-1}}{Y(\phi,n)}\frac{d\phi}{d\eta} \right\}^{\frac{1}{n}}, \tag{3.29}$$

45

where $D^* = [\frac{d^{n+1}m}{\mu^*}]^{\frac{1}{n}}$ has units of length$^{(\frac{n+1}{n})}$ per unit time.

Equation (3.29) is subject to the boundary conditions

$$\phi = \phi_r, \qquad \text{at} \quad \eta = \lambda_s, \tag{3.30}$$

$$\phi = \phi_\ell^*, \qquad \text{at} \quad \eta = \lambda_\ell, \tag{3.31}$$

where $\phi_\ell^* = \phi_r - \frac{p_c}{m}$.

The interface positions can also be expressed as

$$h_s = (\frac{n+1}{n})\lambda_s(D^*t)^{\frac{n}{n+1}}, \qquad h_\ell = (\frac{n+1}{n})\lambda_\ell(D^*t)^{\frac{n}{n+1}}, \tag{3.32}$$

where λ_s and λ_ℓ are liquid and solid interface positions in terms of the similarity variable.

After introducing these relations for interface positions into ODEs for interface position we obtain the following non–linear equations

$$\lambda_s = \left(\frac{n}{n+1}\right)^{\frac{1}{n}} \left[\frac{(1-\phi_0)}{\phi_0} \left\{ \frac{\phi^n W(\phi)}{(1-\phi)Y(\phi,n)} \frac{d\phi}{d\eta}\bigg|_{\lambda_\ell^-} \right\} - \left\{ \frac{(1-\phi^n)W(\phi)}{Y(\phi,n)} \frac{d\phi}{d\eta}\bigg|_{\lambda_s^+} \right\} \right], \tag{3.33}$$

$$\lambda_\ell = \left(\frac{n}{n+1}\right)^{\frac{1}{n}} \left[\frac{1}{\phi_0} \left\{ \frac{\phi^n W(\phi)}{Y(\phi,n)(1-\phi)} \frac{d\phi}{d\eta}\bigg|_{\lambda_\ell^-} \right\}^{\frac{1}{n}} \right]. \tag{3.34}$$

This system of non–linear ODE (3.29) and non–linear equations (3.33,3.34) is solved numerically. We use second order accurate finite difference and mid point rule schemes to discretize in space. This converts the ODE and non–linear system of equations into a system of non–linear equations, which is solved numerically using fsolve in Matlab. This numerically computed solution in the absence of gravity effects is used as an initial condition for the full time dependent problem (see [59] for more details) presented in the next section. The result of the zero gravity case will be shown in the results section.

3.6 Non–zero Gravity Case:

The time–dependent moving domain problem (3.19)–(3.26) can be non–dimensionalized and transformed to a fixed domain by using the following choices for dimensionless space, time, interface positions and pressure

$$\bar{z} = \frac{z - h_s(t)}{h_\ell(t) - h_s(t)}, \qquad \bar{t} = \frac{t}{T}, \qquad \bar{h}_s = \frac{h_s}{L}, \qquad \bar{h}_\ell = \frac{h_\ell}{L}, \qquad \bar{p} = \frac{p}{m}, \qquad (3.35)$$

where $L = \frac{m}{\rho_\ell g}$ and $T^n = \frac{L^{n+1}\mu^*}{md^{n+1}}$. Note that this particular time scale depends on power law index n. We shall revisit this issue in the discussion of the results. Introducing these choices and dimensionless variables, the dimensionless PDE (3.19) for ϕ can be written as

$$\frac{\partial \phi}{\partial \bar{t}} + \left[\frac{(\bar{z} - 1)}{(\bar{h}_\ell - \bar{h}_s)} \frac{d\bar{h}_s}{d\bar{t}} - \frac{\bar{z}}{(\bar{h}_\ell - \bar{h}_s)} \frac{d\bar{h}_\ell}{d\bar{t}} \right] \frac{\partial \phi}{\partial \bar{z}} + \frac{\bar{c}(\bar{t})}{(\bar{h}_\ell - \bar{h}_s)} \frac{\partial \phi}{\partial \bar{z}} =$$

$$\frac{1}{(\bar{h}_\ell - \bar{h}_s)} \frac{\partial}{\partial \bar{z}} \left[\frac{W(\phi)\phi^n(1 - \phi)^{n-1}}{Y(\phi, n)\mu^*} \left\{ \frac{1}{(\bar{h}_\ell - \bar{h}_s)} \frac{\partial \phi}{\partial \bar{z}} + \rho\phi \right\}^{\frac{1}{n}} \right], \qquad (3.36)$$

where $\rho = \left(\frac{\rho_s}{\rho_\ell} - 1 \right)$.

The boundary conditions for solid volume fraction are written as follows

$$\phi = \phi_r, \qquad\qquad\qquad \text{at} \qquad \bar{z} = 0, \qquad (3.37)$$

$$\phi = \phi_\ell^* - (\bar{h}_\ell - \bar{h}_s) \int_0^1 (\rho\phi + 1) d\bar{z} - \bar{h}_s \qquad \text{at} \qquad \bar{z} = 1. \qquad (3.38)$$

It is important to mention that these boundary conditions are same as in Newtonian case [see [59] and chapter 2]. We derive boundary condition (3.38) after the substituting of relation $\sigma = \sigma(\phi)$ in (3.18) and using pressure boundary conditions (3.21) and (3.24). Introducing the choices and dimensionless variables defined in (3.35), reduces the equations for interface

47

positions to

$$\frac{d\bar{h}_s}{d\bar{t}} = \bar{c}(\bar{t}) - \left[\frac{W(\phi)(1-\phi)^{n-1}}{Y(\phi,n)} \left(\frac{1}{(\bar{h}_\ell - \bar{h}_s)} \frac{\partial \phi}{\partial \bar{z}} + \rho\phi \right) \Big|_{\bar{z}=0} \right]^{\frac{1}{n}}, \qquad (3.39)$$

$$\frac{d\bar{h}_\ell}{d\bar{t}} = \bar{c}(\bar{t}) + \left[\frac{W(\phi)\phi^n}{Y(\phi,n)(1-\phi)} \left(\frac{1}{(\bar{h}_\ell - \bar{h}_s)} \frac{\partial \phi}{\partial \bar{z}} + \rho\phi \right) \Big|_{\bar{z}=1} \right]^{\frac{1}{n}}, \qquad (3.40)$$

where the function $\bar{c}(\bar{t})$ is given by

$$\bar{c}(\bar{t}) = \frac{1-\phi_0}{\phi_0} \left[\frac{W(\phi)\phi^n}{Y(\phi,n)(1-\phi)} \left(\frac{1}{(\bar{h}_\ell - \bar{h}_s)} \frac{\partial \phi}{\partial \bar{z}} + \rho\phi \right) \Big|_{\bar{z}=1} \right]^{\frac{1}{n}}. \qquad (3.41)$$

The initial conditions for the interface positions are

$$\bar{h}_\ell(\bar{t}=0) = 0, \qquad \bar{h}_s(\bar{t}=0) = 0. \qquad (3.42)$$

The time dependent free boundary problem (3.36)–(3.42) can be solved numerically. We use a method of lines approach with second order accurate finite difference and mid point rule schemes in space. This converts the PDE to a system of ODEs. The resulting system of ODEs are solved using Matlab's solver ode23s.

3.7 Results and Discussion

The steady state solutions for the non–Newtonian case are same as in Newtonian case. The details on these solutions could be found in [59] and chapter 2. Figure 3.4 shows the evolution of interface positions $\bar{h}_s(t)$ and $\bar{h}_\ell(t)$ in the presence of gravity effects. Again we follow the same approach as in rigid case and introduce the Newtonian time scale $T_{\texttt{New}} = \frac{\mu}{|p_c|}$ in such a way that the time scale used to make these figures is independent of power law index n. This helps to assess the effect of n when examining the graph. In the presence of
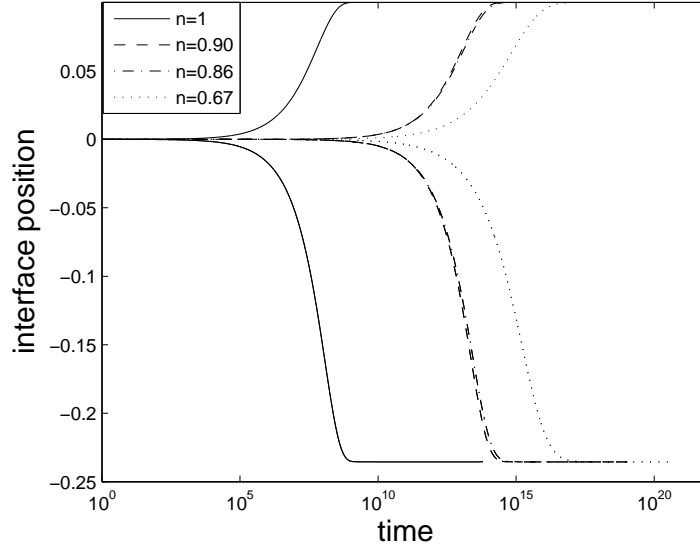
Figure 3.4: This plot shows interface positions as a function of time for Newtonian and shear thinning fluids in the presence of gravity effects. In this plot we have used $\phi_0 = 0.33$, $\phi_r = 0.1$, $\phi_\ell^* = 0.2$ and $\rho = 0.1$. We have also used surface tension $\gamma = 63.57 \times 10^{-3}$ N/m, Newtonian viscosity $= 10^{-3}$ Pa S and particle diameter $d = 0.01$ m. Note that time scale used in this plot is independent of power law index n.

gravity, initially both curves for different power law fluids follow the similarity solution but ultimately reach to an equilibrium height. The Newtonian fluid reaches to an equilibrium height much faster (10^5 time units) than the shear thinning fluid where 10^{14} is 1.573×10^8 sec in actual time unites. The cross over discussed in case of zero gravity rigid porous material occurs in deformable case also but there is no set ordering of this cross over to tell us which fluid imbibes faster than the other. The effect of change in different parameters such as $\phi_0, \phi_r, \phi_\ell^*$ and power law consistency index μ^* values definitely influences the deformation in the solid material and imbibition time. Here again we observe the same trend as in rigid case, by increasing the power law consistency index μ^* values increases the imbibition time and by decreasing the μ^* values decreases the imbibition time. This could be understood by noting that increasing μ^* increases the friction force, which slows the dynamics. In the next figure we show that dependence by using a particular set of parameters ϕ_0, ϕ_r and ϕ_ℓ^*.

Figure 3.5, in which we have used a particular set of parameters from [59] to match with
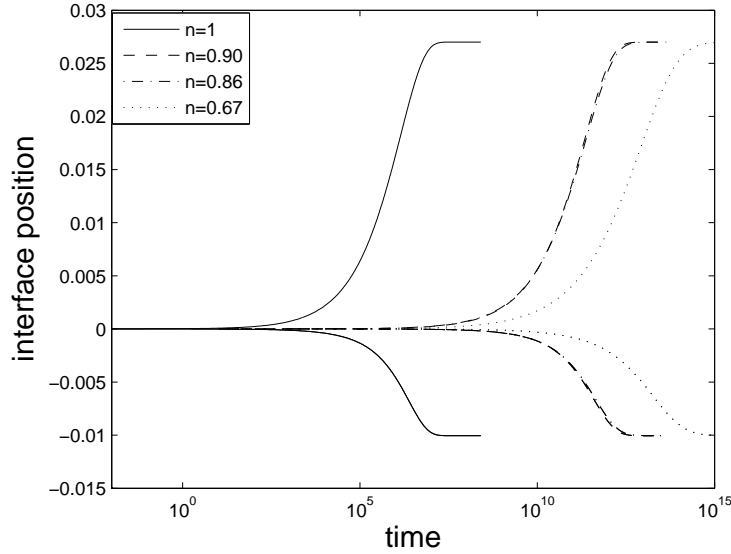
Figure 3.5: This plot shows interface positions versus time for Newtonian and shear thinning fluids. Here we have used $\phi_0 = \phi_\ell^* = 0.10$, $\phi_r = 0.073$ and $\rho = 0.1$.

their sponge experiment, shows less solid deformation than the penetration of liquid into deformable porous material. Again there is a cross over for very early times in general in this case also. For this set of parameters the equilibrium height is different than as shown in Figure 3.4 but the equilibrium height is reached in this case also. Here again when the consistency index μ^* value is increased, the shear thinning liquid takes now much more time to reach to an equilibrium height whereas when μ^* value is decreased, the shear thinning liquid reach to an equilibrium faster.

It is worth mentioning that our model is also valid for shear thickening fluid, but the experimental values that we have found in the literature are for power law consistency index μ^* corresponding to shear thinning fluids.

3.8   Conclusion

We have extended our previous work [59] to a one–dimensional capillary rise of power law fluids into rigid and deformable porous materials. The new contributions here are our model for power law fluids and numerically computed solution for both rigid and deformable cases

50

in the absence and presence of gravity effects. We have used the mixture theory approach to study capillary rise of power law fluids into deformable porous materials. The modeling and solution approach used here is similar to ones in the previous work by the various authors [3; 8; 57; 59].

In, the case of rigid porous materials we have shown the difference in capillary rise of Newtonian and non–Newtonian fluids. We observed that the dynamics of Newtonian and non–Newtonian fluid is different in different time regimes. For really early time imbibition of non–Newtonian fluid is faster than the shear thinning fluids and this trend is opposite for later times. We have shown the intersection time (where the dynamics between different fluid changes) between different fluids in table 3.1.

In the presence of gravity effects, the same equilibrium height is reached for both Newtonian and non–Newtonian liquids. We have observed that the Newtonian fluid reaches to an equilibrium height before the shear thinning liquid for the particular set of values shown in table 3.1. However, the imbibition of the liquid into the porous material depends on various parameters such as Darcy number Da, capillary pressure p_c, uniform volume fraction ϕ_0 and consistency index μ^*. On increasing the Da and p_c values the imbibition of the fluid increases while imbibition decreases if Da and p_c values are decreased. The effect of increasing the power law consistence index μ^* decreases the liquid imbibition and vice versa.

In the deformable case, when gravity effects are present both liquid and solid interface positions reach to an equilibrium heights as shown in figures 3.4 and 3.5. We have used the numerically computed zero gravity solution as an initial condition for nonzero gravity solution. This zero gravity solution follows the square root in time behavior for Newtonian fluid case whereas for non–Newtonian fluids it follows a different power law depending on the power law index n. No steady state solution exists in the absence of gravity effects for both Newtonian and power law fluid cases. When gravity effects are included in the model the steady state solution are same for both Newtonian as well as power law fluids (see [59] for details on this steady solution).

The capillary rise of non–Newtonian liquid into both rigid and deformable porous material cases highlights basic features of this interesting phenomena. The additional features such as multidimensional deformation, evaporation, chemical interaction between liquid and solid phases, and experimental work could be motivated by the present work.

Chapter 4: Mathematical Modeling of Fluid Flow Through a Porous Deformable Arterial Wall

4.1 Introduction

An aneurysm is a localized, blood-filled dilation of the arterial wall caused by disease or weakening of the arterial wall. When the size of an aneurysm increases, there is a high risk of rupture of an aneurysm, which can result in stroke or other complications including sudden death. The interaction between the blood flow and the deformable arterial wall is critical in the understanding of hemodynamic forces such as blood pressure and wall shear stress. Prediction of these forces on and inside the aneurysm arterial wall could better estimate the growth and rupture of arterial wall. In this chapter we will use biphasic mixture theory to study the deformation in the arterial wall which we expect may help us to better understand the growth and rupture of an aneurysm.

There are various theoretical frameworks that have been used to study the biomechanics of arteries and soft tissues: finite elasticity[29; 30], membrane theory [39], viscoelasticity [40; 56], growth and remodeling [20], thermomechanics [28; 47] and mixture theory [4; 15]. In this chapter we want to use the mixture theory approach to model the problem of blood flow interaction within the arterial wall.

Mixture theory has been used to combine continuum theories for the motion and deformation of solid and fluids to model the problems in biological tissues [35; 36; 37], articular cartilage [45; 51], tumor growth and remodeling [17] and other deformable porous materials [2; 3; 6; 7].

Barry and Aldis [6; 7] studied a variety of different models where deformation of the porous material alters the fluid flow. In their flow induced deformation model, biological tissues are modeled as deformable porous media where the deformation of the tissues alters

the fluid motion. They [8] used mixture theory to study the fluid flow over a thin deformable porous layer. In this model they assumed that the solid deformation is infinitesimal and displacements are assumed to be along the axis of the channel.

Other interesting applications where mixture theory has been employed to study the coupled fluid flow and solid deformation problem are paper inkjet printing [3] and infiltration processes [2; 10; 49; 57; 60]. Following this work Siddique et. al [59] studied the capillary rise into deformable porous materials where they were interested in motion of fluid and solid interfaces (see chapter 2 for more details). According to their one dimensional theoretical model, initially both solid and liquid interfaces follow the square in time behavior and ultimately reach to an equilibrium heights. They have also examined the model when gravity and capillary forces are in the same directions. In their experiments they have shown that early time dynamics observed in the experiments are consistent with the early time $t^{1/2}$ dynamics predicted by the theory for capillary rise and material deformation. But their experimental data do not conform the later time equilibrium predictions of our theory.

The above discussion outlines the scientific as well as the industrial application of the mixture theory. We are interested in examining the dynamics of an arterial wall in response to pulsatile fluid flow. In this research we use the basic mixture theory [2; 3; 8] governing equations to model this fluid flow problem.

In section two, we present the general mixture theory formulation. In section three, we present the one dimensional modeling of fluid flow through an arterial wall. In section four, we present the solution of linear elastic membrane problem with linear boundary effects. In section five we present linear elastic membrane problem with non–linear boundary effects. In section six we present solution methodology for fluid flow through arterial wall problem. In section seven and eight we present results and discussion and conclusion of this problem.

4.2   Mathematical Model

We study the fluid structure interaction within the arterial wall using mixture theory. In mixture theory deformable porous material is taken as a continuous binary mixture of fluid and solid phases. The details of mixture theory used in here is similar to one used in [6; 7; 8; 15; 36], Chapter 2 and Chapter 3. When incompressible Newtonian fluid flows through the deformable arterial wall, the porous material deforms and alters the fluid motion through the arterial wall. To take into account both fluid and solid motion the model is stated as conservation of mass and conservation of linear momentum.

The conservation of mass for both fluid and solid phases (we denote here by $\alpha = \ell, s$ respectively), assuming the true intrinsic densities to be constant for mixture ρ_α can be written as

$$\frac{\partial \phi_\alpha}{\partial t} + \nabla.(\phi_\alpha \vec{w}_\alpha) = 0 \tag{4.1}$$

where ϕ_α is solid volume fraction and $\vec{w}_\alpha$ denotes the velocity of each phase in the mixture. Later we will use $\vec{w}_s = \frac{\partial \vec{u}}{\partial t}$ where $\vec{u}$ denotes the displacement of the solid.

The momentum balance for both phases as

$$\rho_\alpha \left(\frac{\partial \vec{w}_\alpha}{\partial t} + \vec{w}_\alpha.\nabla \vec{w}_\alpha \right) = \nabla.\mathbf{T}_\alpha + \vec{\pi}_\alpha, \tag{4.2}$$

where $\mathbf{T}_\alpha$ is the stress tensor for each phase and $\vec{\pi}_\alpha$ is a drag force for each phase.

Assuming the following linear stress–strain relation and incompressible Newtonian fluid

$$\mathbf{T}_s = -\phi p \mathbf{I} + \lambda_s \mathbf{tr}(\mathbf{e}) + 2\mu_s \mathbf{e} \tag{4.3}$$

$$\mathbf{T}_\ell = -(1 - \phi)p \mathbf{I} + \lambda_\ell \mathbf{tr}(\mathbf{D}) + 2\mu_\ell \mathbf{D}, \tag{4.4}$$

where p is the fluid pressure, λ_ℓ, μ_ℓ are the viscous stress constants, λ_s and μ_s are Lame

constants and **I** is the identity tensor. The strain tensor for the solid phase is written as

$$\mathbf{e} = \frac{1}{2}(\nabla \vec{u} + (\nabla \vec{u})^T),$$ (4.5)

where $\vec{u}$ is solid displacement.

The rate strain tensor for the fluid phase is written as

$$\mathbf{D} = \frac{1}{2}(\nabla \vec{w_\ell} + (\nabla \vec{w_\ell})^T).$$ (4.6)

The drag forces for liquid and solid phase are written as

$$\vec{\pi}_\ell = -\vec{\pi}_s = K(\phi)(\vec{w}_s - \vec{w}_\ell) - p\nabla\phi.$$ (4.7)

We neglect the nonlinear $\vec{w}_\ell . \nabla \vec{w}_\ell$ terms in equation (4.2). In the section below we will discuss the fluid structure interaction problem in one dimensional deformable porous arterial wall.

4.3 One dimensional arterial deformation model

In this section we develop a one dimensional mathematical model of fluid flow interactions within the arterial wall. Here we assume that the force from blood pushing against the inner arterial wall is pulsatile. We assume this force provides a sinusoidal displacement with a given amplitude Amp and frequency ω at the inner arterial wall. As a result of the above assumptions and boundary conditions still to be specified, the only unknowns are those inside the arterial wall and the outer boundary position $h(t)$ of the arterial wall. The other variables of interest are the displacement of the solid u, velocity of the liquid w_ℓ, pressure p and the solid volume fraction ϕ. The system of equations (4.1)– (4.2) in one–dimensional

$$\leftarrow z = h(t)$$
$$\leftarrow z = b(t)$$
$$b(t) = Amp \sin \omega t$$
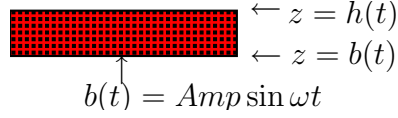
Figure 4.1: This figure shows the schematic of deformable arterial wall

setting reduces to following system of equation

$$\frac{\partial \phi}{\partial t} + \frac{\partial}{\partial z}\left[\phi \frac{\partial u}{\partial t}\right] = 0 \tag{4.8}$$

$$-\frac{\partial \phi}{\partial t} + \frac{\partial}{\partial z}\left[(1 - \phi)w_\ell\right] = 0 \tag{4.9}$$

$$\frac{\partial p}{\partial z} = (\lambda_s + 2\mu_s)\frac{\partial^2 u}{\partial z^2} + 2\mu_a \frac{\partial^2 w_\ell}{\partial z^2} - \rho_s \frac{\partial^2 u}{\partial t^2} - \rho_\ell \frac{\partial w_\ell}{\partial t} \tag{4.10}$$

$$\rho_s \frac{\partial^2 u}{\partial t^2} = (\lambda_s + 2\mu_s)\frac{\partial^2 u}{\partial z^2} - \phi \frac{\partial p}{\partial z} - K\left[\frac{\partial u}{\partial t} - w_\ell\right] \tag{4.11}$$

where the unknowns in the above system of equations are solid displacement u, velocity of the fluid w_ℓ, pressure p and the solid volume fraction ϕ on the moving domain $b(t) < z < h(t)$. Here the position of the outer arterial wall $h(t)$ is moving interface, which we will be computing as an unknown in our model for a given $b(t)$. Here $2\mu_a = \lambda_\ell + 2\mu_\ell$ is the apparent viscosity of the fluid in the porous material.

4.3.1 Boundary Conditions

The boundary conditions applied at the inner side of the arterial wall $z = b(t)$ are

$$u(b(t), t) = b(t), \tag{4.12}$$

$$\frac{\partial u}{\partial t} = w_\ell, \tag{4.13}$$

where we impose $b(t) = Amp \sin \omega t$.

The boundary conditions applied at the outer side of the arterial wall $z = h(t)$ are

$$u(h(t), t) = h(t) - h_0, \tag{4.14}$$

$$\frac{\partial u}{\partial z} = 0, \tag{4.15}$$

$$p(h(t), t) = 0, \tag{4.16}$$

$$\phi(h(t), t) = \phi_r \tag{4.17}$$

where ϕ_r is a relaxed solid volume fraction.

4.3.2 Initial Conditions

At time $t = 0$, we impose that structure displacement and change in the structural displacement with respect to time is zero. Also the solid volume fraction inside the arterial wall is in relaxed state. This leads to the following initial conditions for our system

$$u(z, 0) = 0, \qquad \frac{\partial u}{\partial t} = 0, \qquad \phi(z, 0) = \phi_r,$$

$$b(0) = 0, \qquad h(0) = h_0. \tag{4.18}$$

Adding equations (4.8) and (4.9) and using the boundary conditions (4.13) yields a formula for $w_\ell(z, t)$

$$w_\ell(z, t) = \frac{1}{(1 - \phi)} \left[\frac{db}{dt} - \phi \frac{\partial u}{\partial t} \right], \tag{4.19}$$

which means fluid velocity is known everywhere.

In summary we need to solve (4.8), (4.10) and (4.11) subject to the boundary conditions (4.12)– (4.17) along with appropriate initial conditions (4.18) with w_ℓ given by (4.19). In the next section we will non–dimensionalize the above system of equation along with

58

initial and boundary conditions.

4.3.3 Nondimensionalized system of equations

We introduce the following choices of the dimensionless quantities to non–dimensionalize the above system

$$\acute{z} = \frac{z}{h_0}, \quad \acute{t} = \omega t, \quad \acute{u} = \frac{u}{h_0}, \quad \acute{w}_\ell = \frac{w_\ell}{h_0 \omega}, \quad \acute{h} = \frac{h(t)}{h_0}, \quad \acute{p} = \frac{p}{(\lambda_s + 2\mu_s)}. \tag{4.20}$$

The resulting set of dimensionless equation are given below

$$\frac{\partial \phi}{\partial \acute{t}} + \frac{\partial}{\partial \acute{z}} \left[\phi \frac{\partial \acute{u}}{\partial \acute{t}} \right] = 0 \tag{4.21}$$

$$\acute{w}_\ell(z, t) = \frac{1}{(1 - \phi)} \left[\frac{d\acute{b}}{d\acute{t}} - \phi \frac{\partial \acute{u}}{\partial \acute{t}} \right] \tag{4.22}$$

$$\frac{\partial \acute{p}}{\partial \acute{z}} = \frac{\partial^2 \acute{u}}{\partial \acute{z}^2} + \alpha_\mu \frac{\partial^2 \acute{w}_\ell}{\partial \acute{z}^2} - \alpha_\omega \frac{\partial^2 \acute{u}}{\partial \acute{t}^2} - \alpha_\omega \rho \frac{\partial \acute{w}_\ell}{\partial \acute{t}} \tag{4.23}$$

$$\frac{\partial^2 \acute{u}}{\partial \acute{t}^2} = \alpha_\omega^{-1} \frac{\partial^2 \acute{u}}{\partial \acute{z}^2} - \alpha_\omega^{-1} \phi \frac{\partial \acute{p}}{\partial \acute{z}} - \alpha_k \left[\frac{\partial \acute{u}}{\partial \acute{t}} - \acute{w}_\ell \right] \tag{4.24}$$

where $\alpha_\mu = \frac{2\mu_a \omega}{(\lambda_s + 2\mu_s)}$, $\alpha_\omega^{-1} = \frac{(\lambda_s + 2\mu_s)}{\rho_s \omega^2 h_0^2}$, $\alpha_k = \frac{K}{\rho_s \omega}$ and $\rho = \frac{\rho_\ell}{\rho_s}$. In the next two sections

we will present these models after dropping the primes and their solutions.

4.4 Linear Elastic Membrane with Linear Boundary Effects

We study the simplified linear elastic membrane problem given below

$$\frac{\partial^2 u}{\partial t^2} = \alpha_\omega^{-1} \frac{\partial^2 u}{\partial z^2}, \qquad 0 \leq z \leq 1 \tag{4.25}$$

with the linear boundary effects. We assume that the initial solid displacement and rate of change in solid displacement are zero i.e. $u(z, 0) = 0$ and $\frac{\partial u}{\partial t}(z, 0) = 0$.

We specify the following boundary conditions at the bottom interface of the arterial wall $u(z = 0) = b(t)$ and at the upper interface of the arterial wall we impose the change in the displacement $\frac{\partial u}{\partial z}(z = 1) = 0$. To specify the pulsatile motion at the bottom interface of the arterial wall we set $b(t) = Amp \sin \omega t$.

We solve PDE (4.25) numerically using method of lines. This was accomplished by solving an equivalent system of first–order differential equations

$$\frac{\partial u}{\partial t} = y, \tag{4.26}$$

$$\frac{\partial y}{\partial t} = \alpha_\omega^{-1} \frac{\partial^2 u}{\partial z^2}. \tag{4.27}$$

We use second order finite difference scheme to discretize (4.27) that converts the PDE into a system of ODEs. This system of ODEs is solved numerically using Matlab's ode23 solver. In the Appendix A we present the validation of method of lines for wave equation with an exact solution.

We apply the sinusoidal wave function $Amp \sin t$ on the inner boundary of the arterial wall and compute the solid displacement at the outer arterial wall. Figure 4.2 shows this displacement at $z = 1$ relative to the driving amplitude as function of time. There is no response of outer arterial wall until $t = 1$ (this delay in the disturbance is associated with wave speed of disturbance). After $t = 1$ response begins. The response at $z = 1$ reveals a complex pattern. This disturbance within the arterial wall bounces back and forth. The detailed structure is a function of speed at which disturbance propagates and interacts with driving disturbance as shown in figure 4.7. Note that the amplitude of disturbance is more than three times the size of the driving amplitude. We investigate this further in figure 4.4.
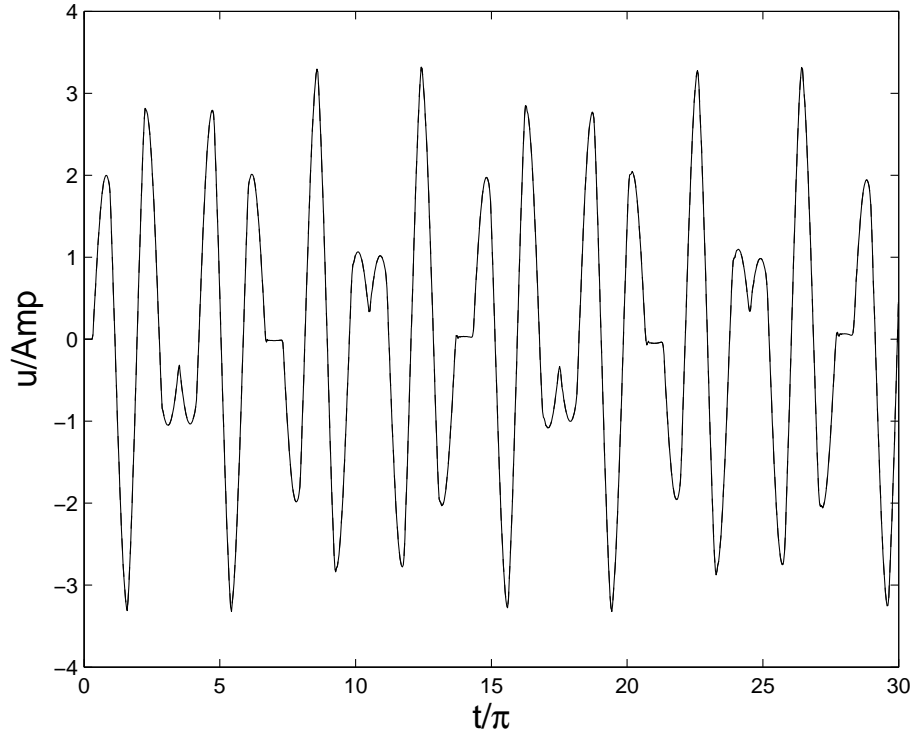
Figure 4.2: This is plot of displacement/Amp as function of time. We have used $Amp = 0.001$ and $\alpha_\omega = 1$ in this case.

Figure 4.3 is surface plot of displacement, space and time relative to the driving amplitude. This figure shows that the disturbance in the arterial wall reaches at $z = 1$ and then responses back to $z = 0$ depending upon the speed and amplitude of the wave. We explore this dependence in figure 4.4.

Figure 4.4 is plot of displacement U_{max} as function amplitude. Here we are interested in potential resonant behavior. Note that when $\alpha_\omega \to 0$, $U_{\max}$ goes to the driving amplitude. Here a small peak exist for small values of α_ω^{-1} and strong peak for large values of α_ω^{-1} (almost 20 times the driving amplitude).
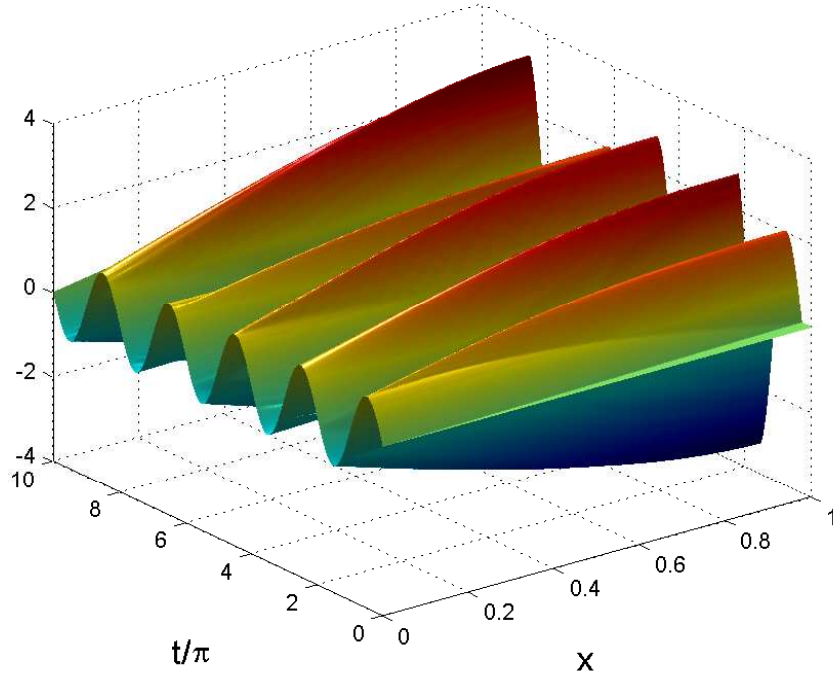
Figure 4.3: This is surface plot of displacement/Amp, space and time. We have used $Amp = 0.001$ and $\alpha_\omega = 1$ in this case.

4.5   Linear Elastic Membrane with non–Linear Boundary Effects

In this case again we study the linear elastic membrane problem

$$\frac{\partial^2 u}{\partial t^2} = \alpha_\omega^{-1}\frac{\partial^2 u}{\partial z^2}, \qquad b(t) \leq z \leq h(t) \tag{4.28}$$

with moving boundary effects. Here again we impose the same initial and boundary conditions with $u(h,t) = h(t) - h_0$, where h_0 is initial thickness of the arterial wall. Below we define a transformation that allow us to transform the moving boundary problem to a fixed domain problem.
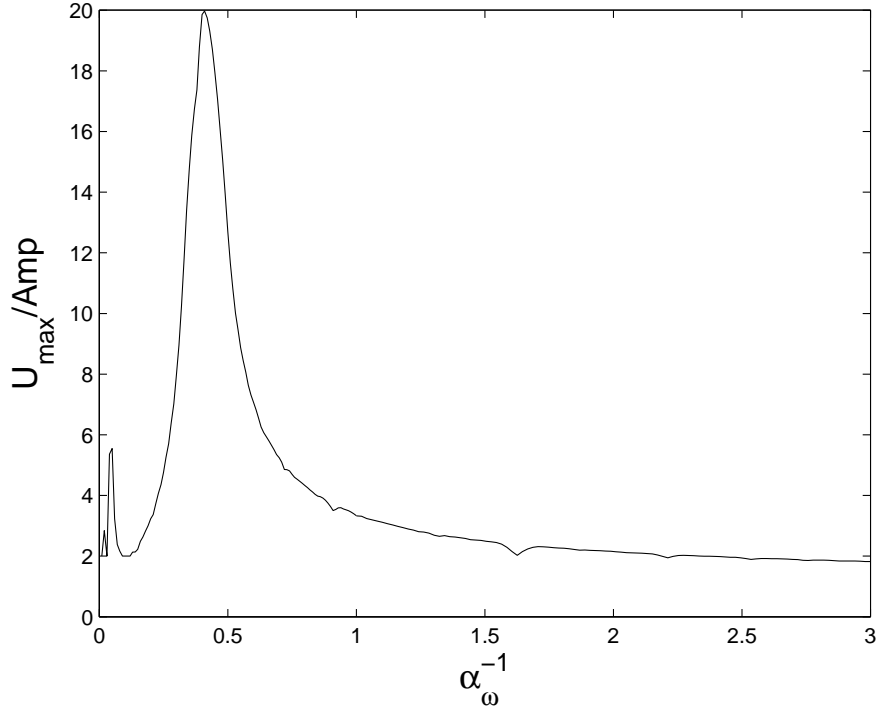
Figure 4.4: This is Umax as function of time. We have used $Amp = 0.001$.

4.5.1 Transformation from moving to fixed domain

The following transformation

$$\bar{z} = \frac{z - b(t)}{b(t) - h(t)}, \qquad \bar{t} = t \tag{4.29}$$

allow us to write the problem on fixed domain $b(t) \leq z \leq h(t)$.

$$\frac{\partial^2 u}{\partial \bar{t}^2} = \alpha_\omega^{-1} P^2(t) \frac{\partial^2 u}{\partial \bar{z}^2} - 2Q \frac{\partial^2 u}{\partial \bar{t} \partial \bar{z}} - Q^2 \frac{\partial^2 u}{\partial^2 \bar{z}} - \left(\frac{\partial Q}{\partial \bar{t}} + Q \frac{\partial Q}{\partial \bar{z}} \right) \frac{\partial u}{\partial \bar{z}} \tag{4.30}$$

$0 \leq \bar{z} \leq 1$. The details on this transformation can be found in Appendix B.

Following the same procedure as in the previous section, we first convert (4.30) to system of first order PDEs in time where we discretize using second order finite difference scheme. Finally we use Matlab ode23 solver to solve this system of differential equations.

In this figure 4.5 we show the displacement at $z = 1$ relative to the driving amplitude as function of time. It is important to mention that for small values of driving amplitude predictions are same as in fixed domain case. Figure 4.2 shows the agreement between fixed and moving domain solution for small values of amplitude. For large values of driving amplitude we see the difference in two solutions. The two solutions are no longer in synch. Again note that the detailed structure is a function of driving amplitude and speed of propagation of disturbance.
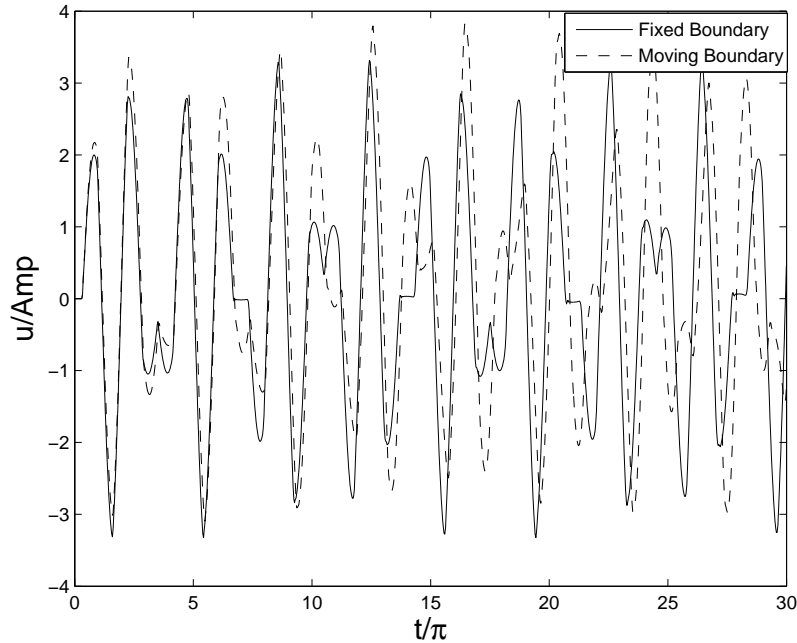
Figure 4.5: This is plot of displacement/Amp as function of time. We have used $Amp = 0.05$ and $\alpha_\omega = 1$ in this case.

4.6 Full Problem Solution

The system of equations (4.21)–(4.24) is transformed from moving domain to a fixed domain using the transformation (4.29). The detailed equations for one dimensional model can be seen in Appendix C.

To solve the system of equations numerically, we first change the second order PDEs in

time to an equivalent system of first–order differential equations in time by following the same procedure as in linear elastic membrane problem with linear and non–linear boundary effects. Again, we use method of lines approach, where we first discretize in space using second order accurate finite difference scheme. Notice that in equation (4.23) and (4.24), w_ℓ and p are function of time but in these two equations w_ℓ and p do not have time derivative terms. Discretization of these PDEs results into a system of differential algebraic equations. We solve this system of differential algebraic equations numerically using Matlab ode15s solver. We have compared our mixture theory code with mixture terms shut off to verify with elastic membrane problem with linear and nonlinear boundary effects. For small driving amplitude these three problems are in good agreement.

4.7   Results and Discussion

In figure 4.6 we plot displacement relative to the driving amplitude as a function of time. There is no delay in response in the full mixture theory case initially as in the case of linear elastic membrane problem. The propagation of the disturbance in this case is regular. In figures 4.7 and 4.8 we turn off the α_k and α_μ parameters and compare the results with the elastic membrane problem for fixed and moving domains. It is worth mentioning that even for small amplitudes differences in the mixture theory solution and elastic model can be observed. Similar observations can be made in figure 4.8 where we have used a large amplitude value. Figure 4.9 shows the plot of thickness of the arterial wall as a function of time. Here we observe small deformation in the arterial wall. The maximum change in thickness is less than the driving amplitude. If the thickness is 1 then there is no deformation. In figure 4.10 we show the flux as a function of time at the outer arterial wall. Note that this assumes a source of fluid exterior to the wall.

In figure 4.11 we plot displacement relative to the driving amplitude as a function of time. For the solid line we turn off the permeability parameter α_k and viscosity parameter α_μ as in figures 4.7 and 4.8. For the dashed dotted line we turn on the permeability parameter α_k. We observe that the delay in the response at the outer arterial wall is modified by
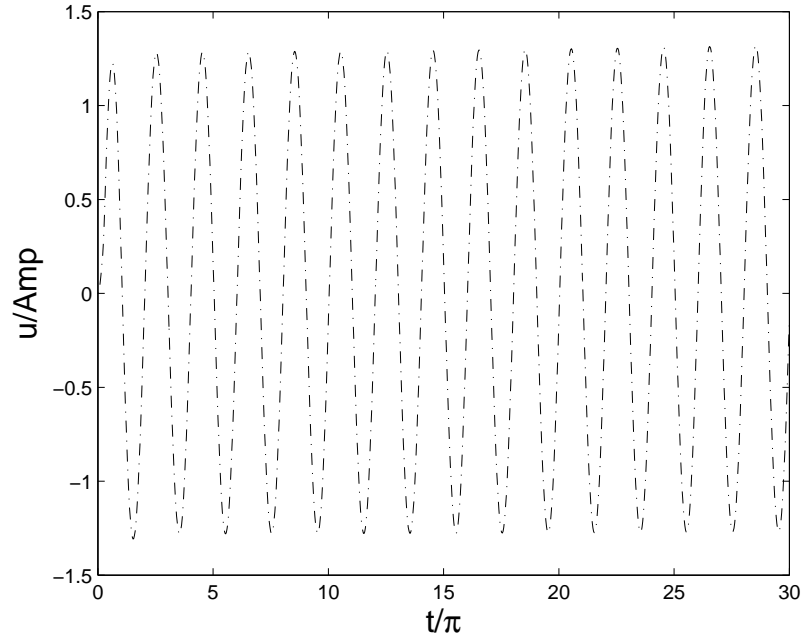
Figure 4.6: This is a plot of displacement/Amp as a function of time. Here we have used $Amp = 0.01$, $\alpha_\omega = 0.7$, $\alpha_k = 0.9$, $\alpha_\mu = 0.5$ and $\rho = 1$.

turning on the permeability parameter α_k. Here we also observed the changes amplitude of the displacement.

Figure 4.12 shows the plot of displacement of the solid relative to the driving amplitude as a function of time. Here, again solid line is the result with permeability α_k and viscosity parameters α_μ set to zero. In the dashed dotted line we turn on the viscosity parameter α_μ. Initially there is no change in response at the outer arterial wall but as time evolves changes in the two solutions are observed.

4.8   Conclusions

In this chapter we have considered a one–dimensional model of fluid flow interaction within a deformable arterial wall. In this model we have used mixture theory approach to compute the displacement of solid and fluid motion. The main focus of this one–dimensional study is to understand the deformation in the arterial wall as function of its material properties.

66
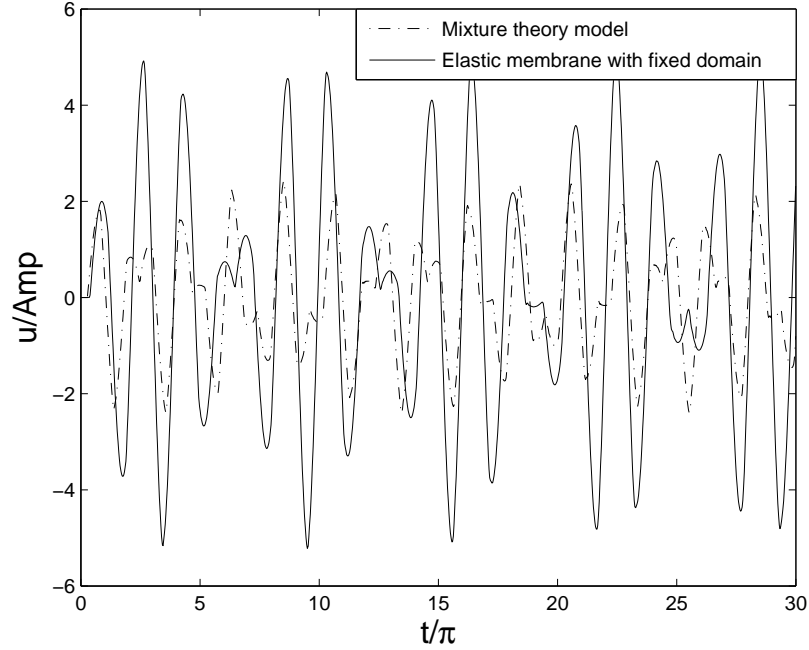
Figure 4.7: This is a plot of displacement/Amp as a function of time. Here we have used $Amp = 0.001$, $\alpha_\omega = 0.7$, $\alpha_k = 0$, $\alpha_\mu = 0$ and $\rho = 1$.

We have used mixture approach to model the one dimensional deformable arterial wall problem. We compare our mixture theory results with elastic membrane with fixed and moving domain problems.

In fixed domain elastic membrane problem we observe a delay in a response at the outer arterial wall. This response at the outer arterial wall reveals a complex structure. The disturbance within the arterial wall bounces around. Here the detailed structure of the disturbance is a function of propagation of the wave. It is also observed that the amplitude of disturbance is a function of driving amplitude.

In moving domain elastic membrane problem the response at the outer arterial wall for the small values of driving amplitude is in good agreement with the fixed domain elastic membrane problem. However, for the large values of driving amplitude we observe that both solution are no longer in phase.

In our full mixture theory model, depending on the parameter values, there may or may not be a delay in the propagation of disturbance. We have assessed the response at the
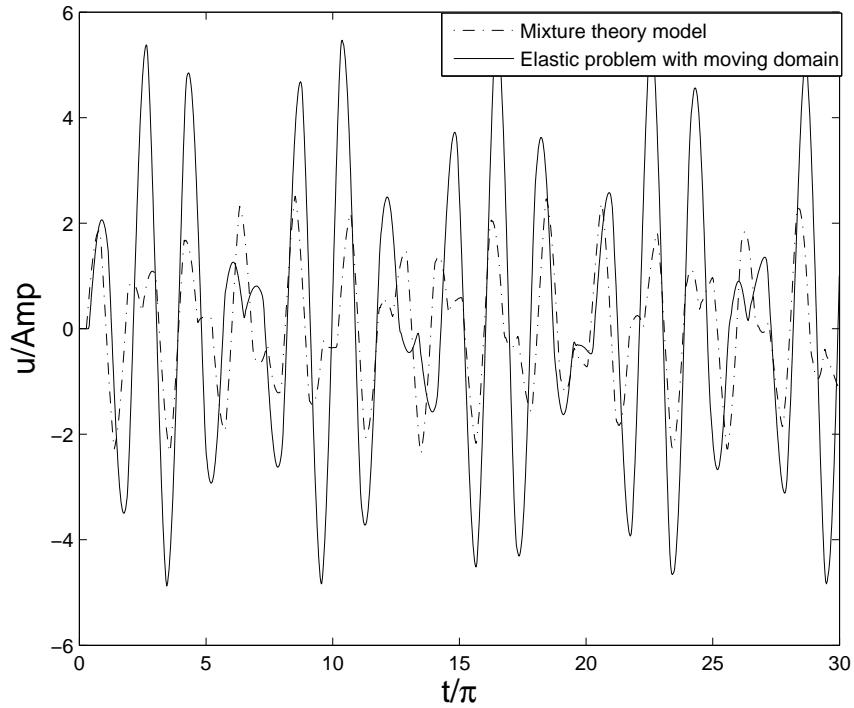
Figure 4.8: This is a plot of displacement/Amp as a function of time. Here we have used $Amp = 0.02$, $\alpha_\omega = 0.7$, $\alpha_k = 0$, $\alpha_\mu = 0$ and $\rho = 1$.

outer arterial wall as well as wall thickness and flux as parameter values varied.

Clearly, we explored the solution for two simple, elastic membrane problems with fixed and moving domain and a mixture theory problem. There is definitely a possibility of exploring further dependence of mixture theory problem parameters. We hope that this work may lead to the better understanding of rupture of the arterial wall.
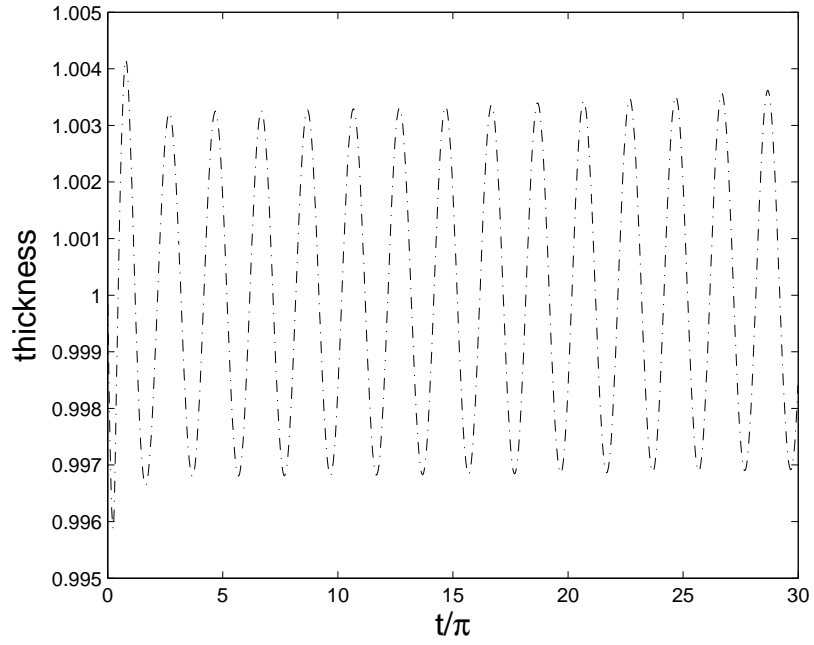
Figure 4.9: This is a plot thickness of arterial wall as function of time. In this plot we have used $Amp = 0.01$, $\alpha_k = 0.9, \alpha_\omega = 0.7$, $\alpha_\mu = 0.5$ and $\rho = 1$.
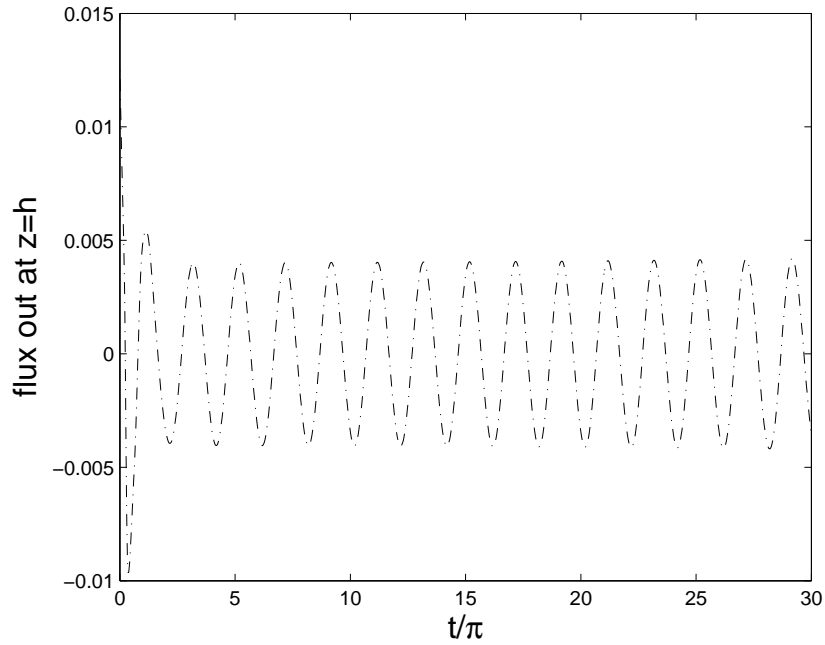
Figure 4.10: This is a plot of flux as function of time. In this plot we have used $Amp = 0.01$, $\alpha_k = 0.9, \alpha_\omega = 0.7$, $\alpha_\mu = 0.5$ and $\rho = 1$
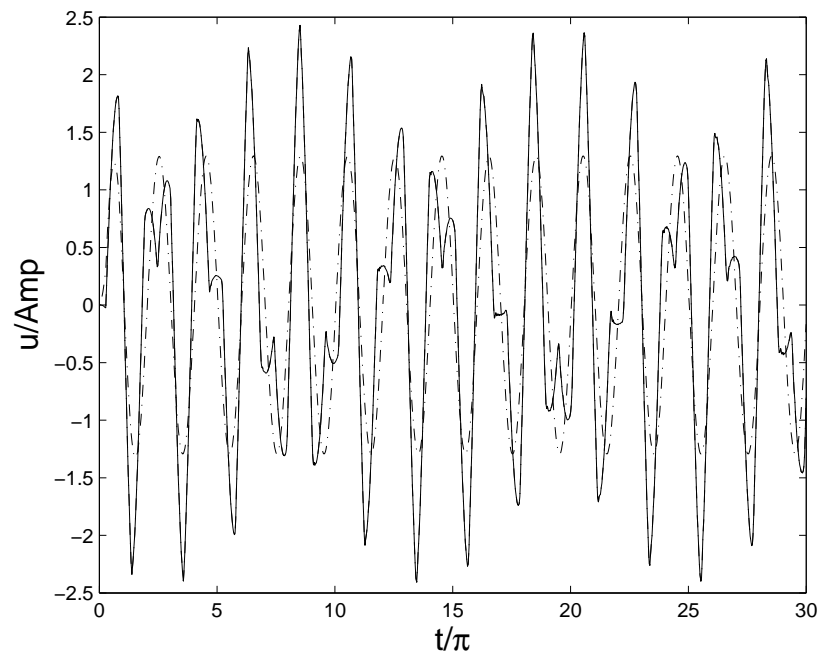
Figure 4.11: This is a plot of displacement as a function of time for mixture theory model for two different sets of parameters. Solid line is a plot for $\alpha_k = 0, \alpha_\omega = 0.7, \alpha_\mu = 0$ whereas dashed dotted line is a plot for $\alpha_k = 0.9, \alpha_\omega = 0.7, \alpha_\mu = 0$. In both of these plots we have used $Amp = 0.001$ and $\rho = 1$.
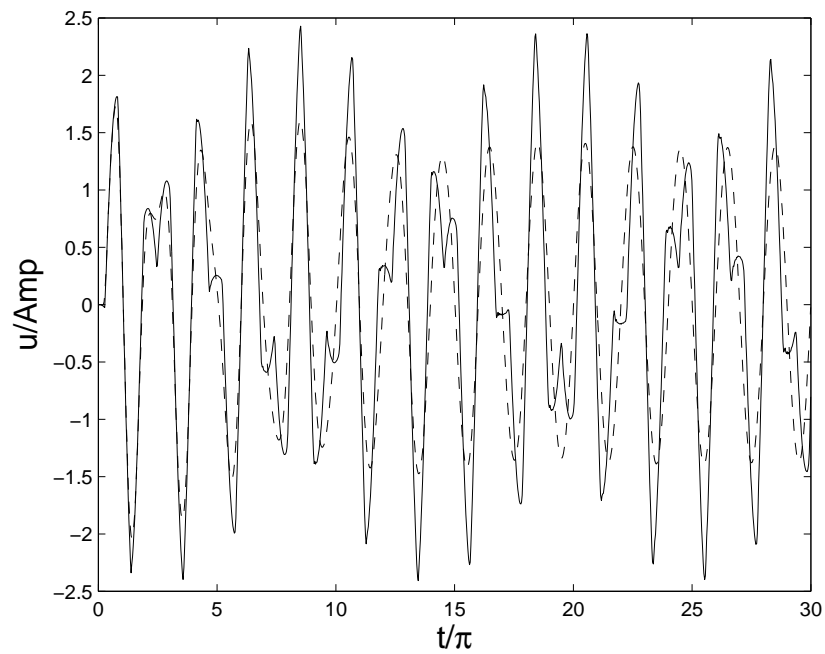
Figure 4.12: This is a plot of displacement as function of time for mixture theory model for two different sets of parameters. Solid line is a plot for $\alpha_k = 0, \alpha_\omega = 0.7$, $\alpha_\mu = 0$ whereas dashed dotted line is a plot for $\alpha_k = 0, \alpha_\omega = 0.7$, $\alpha_\mu = 0.5$. In both of these plots we have used $Amp = 0.001$ and $\rho = 1$.

Chapter 5: Conclusions and Future Work

In this dissertation we have used mixture theory to model problems of fluid flow through deformable porous materials.

We have considered the capillary rise of a fluid into deformable porous material. We have computed the analytical and numerical solution to take into account the gravity and capillarity effects. In their one dimensional model they were interested in computing the solid deformation and imbibition of liquid. In the presence of gravity effects initially both interface positions follow the square root in time behavior and ultimately reach to steady state heights. In our model the fluid motion and deformation in the solid is due to the capillary pressure. When capillary pressure is zero, fluid motion and solid deformation is zero. Increase in the capillary pressure results in increase in the deformation of the porous material. We also observed that the equilibrium rise height of the fluid is same for both rigid and deformable porous material case, assuming the same applied capillary pressure. We also addressed the problem where the capillary pressure and gravitational forces act in the same direction. In this case we observed that the drainage of liquid is faster for nonzero gravity case. Another important result is that the drainage time is inversely proportional to the capillary suction. Our theoretical model helped to guide the experiments (see[59] for more details).

Second, we also studied the capillary rise of non–Newtonian fluid through deformable porous material. In this case we presented the mixture theory based power law fluid model and solutions for both rigid and deformable cases. Here we have shown the difference in the dynamics of Newtonian and non–Newtonian fluids. We observed that for really early time imbibition of non–Newtonian fluid is faster than the Newtonian fluid and this trend is opposite for later time. We hope that our non–Newtonian model will help to guide the experiments.

Finally, we developed a mixture theory based one dimensional mathematical model of fluid flow interactions within the arterial wall. We compared our mixture theory model to the elastic membrane models. For fixed and moving domain elastic membrane problem we observe a complex pattern. The disturbance within the arterial wall moves back and forth. This propagation of disturbance in the arterial wall is a function of driving amplitude and speed of the propagation of wave. We also observed that a small peak of maximum displacement occurs for α_ω^{-1} and a high peak for larger values α_ω^{-1}. For the smaller values of driving amplitude both fixed and moving domain solutions for elastic domain problem are in good agreement. Whereas for the large value these two solutions are no longer in synch with linear predictions. For the full mixture theory problem we observe a regular behavior and a possibly modified delay in response at the outer arterial wall.

We answered many questions in this dissertation using the mixture theory approach. An interesting possible question which we further want to investigate and have not been answered.

5.1 Two dimensional fluid flow through a channel coupled with deformable arterial wall

In this problem we want to study the two dimensional flow through a channel coupled with deformable arterial walls. The geometry of the problem is shown in figure (5.1). Here we have use standard Navier Stokes equations to describe the flow in the channel coupled with mixture theory model describing the fluid structure interaction within the deformable arterial wall.

In purely fluid region, the fluid motion is described by the Navier Stokes equations

$$\nabla.\vec{w}_\ell = 0$$

$$\rho^f \left(\frac{\partial \vec{w}_\ell}{\partial t} + \vec{w}_\ell.\nabla \vec{w}_\ell \right) = -\nabla p + \mu_\ell \nabla^2 \vec{w}_\ell,$$

73
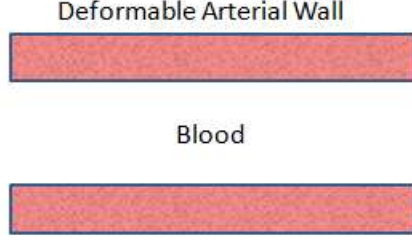
Figure 5.1: This figure shows the schematic of fluid flow in a deformable arterial wall

where $\vec{w}_\ell$ is fluid velocity, p is pressure, ρ^f fluid density and μ^f is fluid viscosity.

In mixture theory porous material is modeled as a continuous binary mixture of liquid and solid phases assuming that each point in space is occupied by both solid and liquid phases. For detailed derivation on mixture theory see [8] and chapters (2 and 4).

The conservation of mass for liquid and solid phase is written as follows

$$\frac{\partial \phi_s}{\partial t} + \nabla \cdot (\phi_s \vec{w}_s) = 0$$

$$\frac{\partial \phi_\ell}{\partial t} + \nabla \cdot (\phi_\ell \vec{w}_\ell) = 0$$

where velocity of solid is related to displacement of solid $\mathbf{u}$ through $\vec{w}_s = \partial \mathbf{u}/\partial t$. The momentum balance for solid and liquid phase after neglecting the gravity effects can be written as

$$\rho_s \left(\frac{\partial \vec{w}_s}{\partial t} + \vec{w}_s \cdot \nabla \vec{w}_s \right) = \nabla \cdot \mathbf{T}_s + \vec{\pi}_s$$

$$\rho_\ell \left(\frac{\partial \vec{w}_\ell}{\partial t} + \vec{w}_\ell \cdot \nabla \vec{w}_\ell \right) = \nabla \cdot \mathbf{T}_\ell + \vec{\pi}_\ell.$$

Where $\mathbf{T}_s$ and $\mathbf{T}_\ell$ are stress tensors for solid and liquid phases, $\vec{\pi}_s$ and $\vec{\pi}_\ell$ are the drag forces. According to Newton's third law the force on the solid constituents is opposite to that on the liquid by the solid which allow us to write $\vec{\pi}_s = -\vec{\pi}_\ell$.

For the definitions of the stresses we follow Barry and Aldis [8]

$$\mathbf{T}_s = -\phi p\mathbf{I} + \lambda_s \mathbf{tr}(\mathbf{e}) + 2\mu_s \mathbf{e} \tag{5.1}$$

$$\mathbf{T}_\ell = -(1-\phi)p\mathbf{I} + \lambda_\ell \mathbf{tr}(\mathbf{D}) + 2\mu_\ell \mathbf{D}, \tag{5.2}$$

where λ_ℓ, μ_ℓ are the viscous stress constants, λ_s and μ_s are Lame constants, $\mathbf{I}$ is the identity tensor and p is the pressure.

We impose the following matching boundary conditions representing the conservation of mass and linear momentum at fluid–porous medium interface

$$\|\phi^f(\vec{w}_\ell - \vec{w}_s)\|.\mathbf{n} = 0$$

$$\|\phi^f(\mathbf{T}^s + \mathbf{T}^\ell) - \rho^f \vec{w}_\ell(\vec{w}_\ell - \vec{w}_s)\|.\mathbf{n} = 0,$$

where $\|\cdot\|$ is the jump going from fluid only region to the porous deformable medium. Here $\mathbf{n}$ is the normal unit vector at the interface pointing into the fluid region. To close the system we need to specify the boundary and initial conditions which is in progress. Here we hope that parameter estimation may lead us to the better understanding of the rupture of an arterial wall.

Appendix A: Test Problem:

We have used method of lines to solve the elastic membrane problem. In Appendix A we want to verify that method on a simple wave equation that admits an analytical solution

$$\frac{\partial^2 u}{\partial t^2} = \frac{\partial^2 u}{\partial z^2}, \quad 0 < z < 1, 0 < t;$$

$$u(0, t) = u(1, t) = 0, 0 < t,$$

$$u(z, 0) = \sin \pi z, \quad 0 \leq z \leq 1,$$

$$\frac{\partial u}{\partial t}(z, 0) = 0, \quad 0 \leq z \leq 1,$$

with actual solution

$$u(z, t) = \cos \pi t \sin \pi z.$$

In this method we first discretize in space using second order finite difference scheme. Tabel B.1 in Appendix A shows that our scheme admits the required order of accuracy.

Table B.1: This table shows the convergence rate α with respect to spatial discretization

N	error=$|U_{\text{approximate}} - U_{\text{exact}}|$	α
26	0.5008	1.6726
50	0.1571	1.9628
100	0.0403	1.9964
200	0.0101	-

Appendix B: Transformation

In this dissertation we are dealing with moving domain problem. To avoid dealing with moving of the interior grid at each time step we use the following transformation to transform the problem on the fixed domain.

$$\bar{z} = \frac{\acute{z} - \acute{b}(t)}{\acute{h}(t) - \acute{b}(t)} \qquad \bar{t} = \acute{t}.$$

This allows us to write

$$\frac{\partial}{\partial \acute{t}} = \frac{\partial}{\partial \bar{t}} + \left[\frac{\bar{z} - 1}{(\acute{h}(t) - \acute{b}(t))} \frac{d\acute{b}(t)}{d\acute{t}} - \frac{\bar{z}}{(\acute{h}(t) - \acute{b}(t))} \frac{d\acute{h}(t)}{d\acute{t}} \right] \frac{\partial}{\partial \bar{z}}, \tag{B.1}$$

Let

$$P(t) = \frac{1}{\acute{h}(t) - \acute{b}(t)}$$

$$\frac{\partial}{\partial z} = P(\bar{t}) \frac{\partial}{\partial \bar{z}} \tag{B.2}$$

$$\frac{\partial^2}{\partial \acute{z}^2} = P^2(\bar{t}) \frac{\partial^2}{\partial \bar{z}^2} \tag{B.3}$$

$$Q(\bar{z}, \bar{t}) = \left[\frac{\bar{z} - 1}{(\acute{h}(t) - \acute{b}(t))} \frac{d\acute{b}(t)}{d\acute{t}} - \frac{\bar{z}}{(\acute{h}(t) - \acute{b}(t))} \frac{d\acute{h}(t)}{d\acute{t}} \right]$$

$$\frac{\partial^2}{\partial \acute{t}^2} = \frac{\partial^2}{\partial \bar{t}^2} + 2Q(\bar{z}, \bar{t}) \frac{\partial^2}{\partial \bar{z} \partial \bar{t}} + Q^2(\bar{z}, \bar{t}) \frac{\partial^2}{\partial \bar{z}^2} + \left(\frac{\partial Q(\bar{z}, \bar{t})}{\partial \bar{t}} + Q(\bar{t}, \bar{t}) \frac{\partial Q(\bar{t}, \bar{t})}{\partial \bar{z}^2} \right) \frac{\partial}{\partial \bar{z}} \tag{B.4}$$

We have used (B.1)– (B.4) to transform all three problems from moving domain to a fixed domain.

Appendix C: Mixture Theory Transformed Equations

The system of equations (4.21)–(4.24) after transforming from moving domain to a fixed domain after dropping the primes can be written as

$$\frac{\partial \phi}{\partial t} + Q\frac{\partial \phi}{\partial z} + P(t)\frac{\partial}{\partial z}\left[\phi(\frac{\partial u}{\partial t} + Q\frac{\partial u}{\partial z})\right] = 0, \tag{C.1}$$

$$v(z,t) = \frac{1}{(1-\phi)}\left[\frac{db}{dt} - \phi(\frac{\partial u}{\partial t} + Q\frac{\partial u}{\partial z})\right], \tag{C.2}$$

$$P(t)\frac{\partial p}{\partial z} = P^2(t)\frac{\partial^2 u}{\partial z^2} + P^2(t)\alpha_\mu \frac{\partial^2 v}{\partial z^2} - \alpha_\omega \left[\frac{\partial^2 u}{\partial t^2} + 2Q\frac{\partial^2 u}{\partial z\partial t} + Q^2\frac{\partial^2 u}{\partial z^2} + \left(\frac{\partial Q}{\partial t} + Q\frac{\partial Q}{\partial z}\right)\frac{\partial u}{\partial z}\right]$$

$$- \alpha_\omega \rho \left(\frac{\partial v}{\partial t} + Q\frac{\partial v}{\partial z}\right), \tag{C.3}$$

$$\frac{\partial^2 u}{\partial t^2} = \alpha_\omega^{-1}P^2(t)\frac{\partial^2 u}{\partial z^2} - \alpha_\omega^{-1}P(t)\phi\frac{\partial p}{\partial z} - \alpha_k \left(\frac{\partial u}{\partial t} + Q\frac{\partial u}{\partial z} - v\right)$$

$$- \left[2Q\frac{\partial^2 u}{\partial t\partial z} + Q^2\frac{\partial^2 u}{\partial z^2} + \left(\frac{\partial Q}{\partial t} + Q\frac{\partial u}{\partial z}\right)\frac{\partial u}{\partial z}\right]. \tag{C.4}$$

This system of equations is solved numerically using method of lines for the full mixture theory model.

Bibliography

Bibliography

[1] T. Al-Fariss and K. L. Pinder, *Flow through porous media of a shear thinning liquid with a yield stress*, Canadian Journal of Chemical Engineering **65** (1987), 391–405.

[2] D. Ambrosi and L. Preziosi, *Modeling injection modeling processes with deformable porous performs*, SIAM J. Appl. Math. **61** (2000), 22–42.

[3] D. M. Anderson, *Imbibition of a liquid droplet on a deformable porous substrate*, Phys. Fluids **17** (2005), 087104.

[4] R. J. Atkin and R. E. Crain, *Continum theories of mixture: Basic theory and historical development*, Quart. J. Mech. Appl. Math. **29** (1976), 209–244.

[5] M. T. Balhoff and K. E. Thompson, *A macroscopic model for shear–thinning flow in packed beds based on network modeling*, Chemical Engineering Science **61** (2006), 698–719.

[6] S. I. Barry and G. K. Aldis, *Flow induced deformation from pressurized cavities in absorbing porous tissues*, Bull. Math. Biol. **54** (1992), 977–997.

[7] _____, *Radial flow through deformable porous shells*, J. Austral. Math. Soc. Ser. B **34** (1993), 333–354.

[8] S. I. Barry, K. H. Parker, and G. K. Aldis, *Fluid flow over a thin deformable porous layer*, Journal of Applied Mathematics and Phys(ZAMP) **42** (1991), 633–648.

[9] Jacob Bear, *Dynamics of Fluids in Porous Media*, second ed., Dover Publications, Inc, New York, 1972.

[10] L. Billi and A. Farina, *Unidirectional infiltration in deformable porous media: Mathematical modeling and self-similar solution*, Q. Appl. Math. **58** (2000), 85–101.

[11] M. A. Biot, *Consolidation settlement under a rectangular load distribution*, J. Appl. Phys. **12** (1941), 426–430.

[12] _____, *General theory of three dimensional consolidation*, J. Appl. Phys. **12** (1941), 155–164.

[13] M. A. Biot and F. M. Clingan, *Consolidation settlement of a soil with an imperveous top surface*, J. Appl. Phys. **12** (1941), 578–581.

[14] R. B. Bird, W. E. Stewart, and E. N. Lightfoot, *Transport phenomena*, Wiley, New York, 1960.

[15] M. R. Bowen, *Incompressible porous media models by use of the theory of mixtures*, Int. J. Engng. Sci. **18** (1980), 1129.

[16] Graham Buckton, *Assessment of the wettability of pharmaceutical powders*, J. Adhesion Sci. and Technol, **7** (1993), 205–219.

[17] H. Byrne and L. Preziosi, *Modeling solid tumor growth using the theory of mixtures*, Mathematical Medicine and Biology **20** (2003), 341–366.

[18] K. S. A. Chen and L. E. Scriven, *Liquid penetration into a deformable porous substrate*, Tappi J. **73** (1990), 151–161.

[19] R. H. Christopher and S. Middleman, *Power-law flow through a packed tube*, Ind. Engng. Chem. Fundls **4** (1965), 422–426.

[20] J. C. Chuong and Y. C. Fung, *On residual stress in arteries*, ASME J. Biomech. Engng **108** (1986), 189–192.

[21] S. H. Davis and L. M. Hocking, *Spreading and imbibition of viscous liquid on a porous base*, Phys. Fluids **11** (1999), 48–57.

[22] _____, *Spreading and imbibition of viscous liquid on a porous base. ii*, Phys. Fluids **12** (2000), 1646–1655.

[23] T. Delker, D. B. Pengra, and P. Wong, *Interface pinning and the dynamics of capillary rise in porous media*, Phys. Rev. Lett. **76** (1996), 2902.

[24] E. R. Dufresne, E. I. Corwin, J. Ashmore N. A. Greenblatt, D. Y. Wang, A. D. Dinsmore, J. X. Cheng, X. S. Xie, J. W. Hutchinson, , and D. A. Weitz, *Flow and fracture in drying nanoparticle suspensions*, Physical Review Letters **91** (2003), 224501.

[25] E.R. Dufresne, D.J. Stark, N.A. Greenblatt, J.X. Cheng, J.W. Hutchinson, L. Mahadevan, and D.A. Weitz, *Dynamics of fracture in drying suspensions*, Langmuir **22** (2006), 7144–7147.

[26] J. Feng and S. Weinbaum, *Lubrication theory in highly compressible porous media: the mechanics of skiing from red cells to humans*, J. Fluid Mech. **422** (2000), 281–317.

[27] A. D. Fitt, P. D. Howell, J. R. King C. P. Please, and D. W. Schwendeman, *Multiphase flow in a roll press nip*, Eur. J. Appl. Math. **13** (2002), 225–259.

[28] J. P. Flory, *Theory of elastic mechanisms in fibrous proteins*, J. Am. Chem. Soc. **78** (1956), 5222–5235.

[29] Y. C. Fung, *Elasticity of soft tissues in simple elongation*, Am. J. Physiol. **28** (1967), 1532–1544.

[30] _____, *Biorheology of soft tissues*, Biorheology **10** (1973), 139–155.

[31] T. D. Hansford, W. J. D. Grant, and M. J. Newton, *The influence of processing variables on the wetting properties of a hydrophobic powder*, Powder Technology, **26** (1980), 119.

[32] R. E. Hayes, A. Afacan, B. Boulanger, and A. V. Shenoy, *Modelling the flow of power law fluids in a packed bed using a volume–averaged equation of motion*, Transport in porous media **23** (1996), 175–196.

[33] M. H. Holmes, *A nonlinear diffusion equation arising in the study of soft tissue*, Q. Appl. Math. **41** (1983), 209–218.

[34] _____, *Comparison theorems and similarity solution approximations for a nonlinear diffusion equation arising in the study of soft tissue*, SIAM J. Appl. Math. **44** (1984), 545–556.

[35] _____, *A theoretical analysis for determining the nonlinear hydraulic permeability of a soft tissue from a permeation experiment*, Bull. Math. Biol. **47** (1985), 669–683.

[36] _____, *Finite deformation of soft tissue: analysis of a mixture model in uni-axial compression*, J. Biomech. Eng. **108** (1986), 372–381.

[37] M. H. Holmes and V. C. Mow, *The nonlinear characteristic of soft gels and hydrated connective tissue in ultrafiltration*, J. Biomech. **23** (1990), 1145–1156.

[38] J. S. Hou, M. H. Holmes, W. M. Lai, and V. C. Mow, *Boundary conditions at the cartilage-synovial fluid interface for joint lubrication and theoretical verifications*, J. Biomechanics Engng. **111** (1989), 78–87.

[39] D. J. Humphery, *Computer method in membrane biomechanics*, Comput. Meth. Biomech. Biomed. Engng **1** (1998), 171–210.

[40] A. G. Johnson, A. G. Livesay, Y. L. S. Woo, and R. K. Rajagopal, *A single intergral finite strain viscoelastic model of ligaments and tendons*, ASME J. Biomech. Engng. **118** (1996), 221–226.

[41] M. Kaczmarek, *Chemically induced deformation of a porous layer coupled with advective-dispersive transport. analytical solutions*, Int. J. Numer. Analyt. Meth. Geomech. **25** (2001), 757–770.

[42] M. Kaczmarek and T. Hueckel, *Chemico-mechanical consolidation of clays: Analytical solutions for a linearized one-dimensional problem*, Transp. Porous Media **32** (1998), 49–74.

[43] Z. Kemblowski and M. Michniewicz, *A new look at the laminar flow of power law fluids through granular beds*, Rheol. Acta **18** (1979), 730–739.

[44] C. Kim, Y. Liu, A. Kühnle, S. Hess, S. Viereck, T. Danner, L. Mahadevan, and D.A. Weitz, *Gravational stability of suspensions of attractive colloidal particles*, Phys. Rev. Lett. (2007), no. 99, 028303.

[45] M. K. Kwan, W. M. Lai, and V. C. Mow, *A finite deformation theory for cartilage and other soft hydrated connective tissues–i. equilibrium results*, J. Biomechanics **23** (1990), 145–155.

[46] M. Lago and M. Araujo, *Capillary rise in porous media*, Journal of Colloid and Interface Science **238** (2000), 35.

[47] W. R. Lawton, *The thermoelastic behavior of isolated aortic strips of the dog*, Circ. Res. **2** (1954), 344–353.

[48] S. Manley, J. M. Skotheim, L. Mahadevan, and D.A. Weitz, *Gravational collapse of colloidal gels*, Phys. Rev. Lett. (2005), no. 94, 218302.

[49] V. J. Michaud, J. L. Sommer, and A. Mortensen, *Infiltration of fibrous performs by a pure metal: Part v. influence of perform compressibility*, Metall Mater. Trans. A **30** (1999), 471–482.

[50] K. A. Missirlis, D. Assimacopoulos, E. Mitsoulis, and R. P. Chhabra, *Wall effects for motion of spheres in power–law fluids*, J. Non–Newtonian Fluid Mech. **96** (2001), 459–471.

[51] V. C. Mow, S. C. Kuei, W. M. Lai, and C. G. Armstrong, *Biphaisc creep and stress relaxation of articular cartilage in compression: theory and experiments*, ASME J. Biomechanical Engng. **102** (1980), 73–83.

[52] H. Pascal, *Rheological behavior effects of non–newtonian fluids on dynamics of moving interface in porous media*, Int. J. Engng Sci. **22** (1984), 227–241.

[53] H. Pascal and F. Pascal, *Flow of non–newtonian fluid through porous media*, Int. J. Engng Sci. **23** (1985), 571–585.

[54] G. P. Peters and D. W. Smith, *Solute transport through a deforming porous medium*, Int. J. Numer. Analyt. Meth. Geomech. **26** (2002), 683–717.

[55] I. Pezron, G. Bourgain, and D. Quéré, *Imbibition of a fabric*, J. Colloid Interface Sci., **173** (1995), 319–327.

[56] P. D. Pioletti and R. L. Rakotomanana, *Non–linear viscoelasticity laws for soft biological tissues*, Eur. J. Mech. A **19** (2000), 749–759.

[57] L. Preziosi, D. D. Joseph, and G. S. Beavers, *Infiltration of initially dry, deforamable porous media*, Int. J. Multiphase Flow **22** (1996), 1205–1222.

[58] T. J. Sadowski, Ph.D. thesis, University of Wisconsin, Madison, Wis, 1963.

[59] Javed Siddique, Daniel Anderson, and Andrei Bondarev, *Capillary rise of fluid into a*

deformable porous materials, Phys. Fluids **21** (2009), 013106.

[60] J. L. Sommer and A. Mortensen, *Forced unidirectional infiltration of deformable porous media*, J. Fluid Mech. **311** (1996), 193–217.

[61] M. Spiegelman, *Flow in deformable porous media. part 1. simple analysis*, J. Fluid Mech. **247** (1993), 17–38.

[62] D. Teeuw and F. T. Hesselink, *Power–law flow and hydrodynamics behavior of biopolymer solutions in porous media*, SPE 8982, Presented at the Fifth Intenational Symposium on Oilfield and Geothermal Chemistry in Stanford, California (1980), 73–86.

[63] W. Wang and K. H. Parker, *The effect of deformable porous surface layers on the motion of a sphere in a narrow cylindrical tube*, J. Fluid Mech. **283** (1995), 287–305.

[64] E. W. Washburn, *The dynamics of capillary flow*, Phys.Rev. **17** (1921), 273–283.

[65] Duncan-Hewitt Wendy and Nisman Rozalia, *Investigation of the surface free energy of pharmaceutical materials from contact angle, sedimentation, and adhesion measurements*, J. Adhesion Sci. and Technol, **7** (1993), 263–283.

[66] B. V. Zhmud, F. Tiberg, and K. Hallstensson, *Dynamic of capillary rise*, Journal of Colloid and Interface Science **228** (2000), 263.

Curriculum Vitae

Javed Iqbal Siddique graduated from the University of Azad Jammu and Kashmir, Muzaffarabad, Pakistan in 1998 . He earned his Master of Philosophy from Quaid-i-Azam University, Islamabad, Pakistan in 2001. He was employed as a Research Associate at COMSATS Institute of Information Technology (CIIT) for two years.

He received his MS in Mathematics from Western Illinois University, Macomb IL in 2004. He has taught variety of undergraduate courses both at Western Illinois University, Marshall Community and Technical College and George Mason University during his studies.

He has accepted a tenure track position as Assistant Professor of mathematics at Penn State, York, starting Fall 2009.